IV. Flight Computers and Sequencers

GUIDANCE AND CONTROL DIVISION

A. Automatic Roving Vehicle Computer Development, *L. Y. Lim*

1. Introduction

The overall objective of this effort is the design and development of an on-board computer for an automatic roving vehicle. The development of an on-board computer requires a detailed knowledge of the various computational tasks that the computer must perform. One of these computational requirements is the navigation of the vehicle.

This report deals with the development of a computational algorithm for the navigation of the vehicle, i.e., a pathfinding algorithm. The detailed presentation on this subject has been published as a technical report (Ref. 1).

2. The Pathfinding Algorithm

The pathfinding algorithm derived in Ref. 1 assumes that: (1) there exists at least one path between the starting position and the target position; (2) each obstacle has contour lines and finite dimensions, and (3) the vehicle has terrain sensors which can detect its immediate surrounding.

Definition 1. An acceptable point is defined as a point (X,Y) such that $|F(X,Y)| \leq E$, where $F(X,Y)$ is a continuous function that describes the terrain, and E is the elevation limit.

Definition 2. A path is defined as a route that connects two points (X_i, Y_i) and (X_j, Y_j) such that the elevation of each point on the route is $|F(X,Y)| \leq E$.

Definition 3. An obstacle is defined as a finite bounded region of a function whose amplitude or values are greater than E, i.e.,

$$|F(X,Y)| \geq E$$

Let $P_0 = (X_0,Y_0)$ and $P_n = (X_n,Y_n)$ be the starting position and the target position on an unknown terrain. Let there exist at least one path connecting P_0 and P_n. The procedures for finding a path which connects P_0 and P_n are:

Step 0. Define

$$d_m = [(X_n - X_0)^2 + (Y_n - Y_0)^2]^{1/2}$$

Step 1. From P_0 go directly to P_n if there are no obstacles between the starting point and the target point. Every point generated in this case is an acceptable point, and every d_i generated is such that $d_j < d_i$ where $j > i$ and

$$d_i = [(X_n - X_{i-1})^2 + (Y_n - Y_{i-1})^2]^{1/2}$$

However, if there is an obstacle encountered at $P_k = (X_k, Y_k)$, replace d_m by d_k, then go to step 2.

Step 2. At point P_k, scan alternately right then left at appropriate increments until an acceptable point is found. Let P_{k+1} be the acceptable point. If $d_{k+1} < d_k$, replace d_m by d_k and P_0 by P_{k+1} go back to step 1. If $d_{k+1} \geqslant d_k$, go to step 3.

Step 3. Determine whether the point P_{k+1} was the result of scanning right or scanning left. If P_{k+1} was the result of the right scanning process, stay on the right contour of the obstacle. Similarly, if P_{k+1} was determined from the left scanning process, stay on the left contour of the obstacle. In either case the right or left contour is followed until an acceptable point $P_q = (X_q, Y_q)$ satisfies the relationship $d_m > d_q$. Once this relationship has been satisfied, replace d_m by d_q and P_0 by P_q, then return to step 1. The process is repeated until P_n is reached.

3. Application

A computer program was coded in Fortran IV language as implemented in the IBM 7090/94 IBJOB system. Examples and results are contained in Ref. 1. The terrain used in all simulations consisted of gaussian density functions. Figure 1 shows a perspective drawing of a gaussian terrain. Figure 2 shows a sample of the results contained in Ref. 1. The algorithm developed under this task does not require *a priori* information about the map in order to find a navigating route; it requires only local terrain information. However, the determined navigational route is not necessarily the optimum one (minimum distance, etc.).

4. Future Plans

Future tasks will include the following:

(1) Determination of the minimum distance navigational route by using terrain information obtained from orbital reconnaissances.

(2) Development of a computational algorithm for the preprocessing of terrain sensor data.

(3) Incorporation into the present algorithm of the ability to "learn" from its experiences as it navigates on the unknown terrain. This might include such factors as statistical classification of the terrain.

Reference

1. Lim, L. Y., *A Pathfinding Algorithm for a Myopic Robot*, Technical Report 32-1288, Jet Propulsion Laboratory, Pasadena, Calif., Aug. 1, 1968.

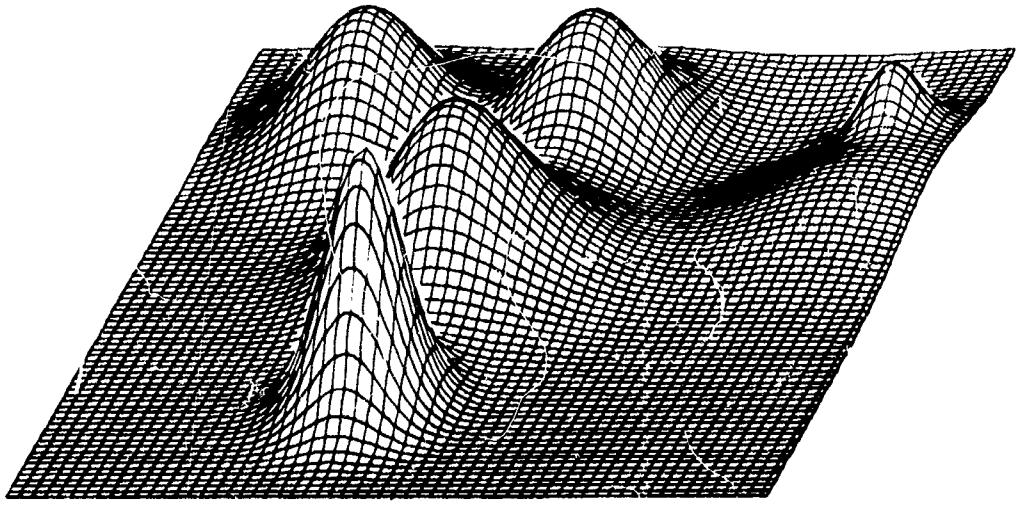

Fig. 1. Perspective drawing of contour configuration

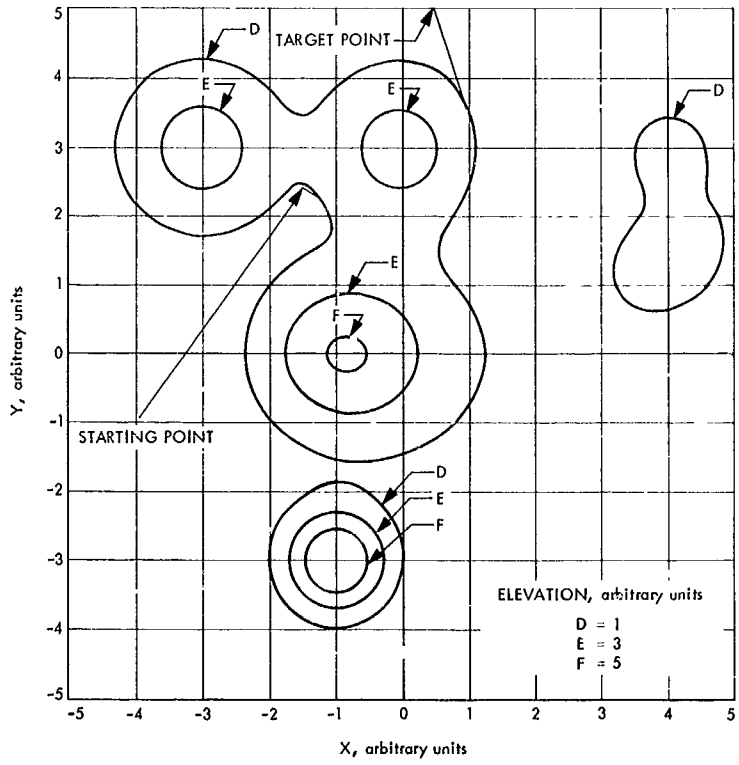

Fig. 2. A simple box canyon configuration

V. Spacecraft Power

GUIDANCE AND CONTROL DIVISION

A. Effect of Electrolyte Concentration on the Electrical Characteristics of AgO–Zn,

R. S. Bogner and R. Patterson

1. Introduction

As part of the JPL advanced battery systems development program, AgO–Zn cells were obtained from Delco-Remy Div. of General Motors Corp. with 40, 45, and 50% concentrations of KOH electrolyte in order to study the effects of concentration on cycle life and electrical performance. The cells were rated by the manufacturer at 25 A-h nominal and were identical in construction except for the electrolyte concentration. The tests were conducted on three 5-cell groups.

2. Experimental Procedure

The cells were charged at 1.5 A for the first seven cycles, and the remaining charge cycles were accomplished at 2.0 A to a minimum cutoff of 1.98 V. All charging was done at room ambient temperature, 75°F, after a minimum 16-h stand period to equilibrate cell temperature.

For the 12 discharge cycles measured, the discharges were made in the order of 2, 10, 30, and 50 A at ambient temperatures of 75, 30, and 100°F. Cell temperature was monitored during the discharge by a transducer mounted on the terminal of one cell in each group. In all instances, the cells were allowed to equilibrate at the ambient discharge temperature for a minimum of 16 h. At the low discharge currents (2 and 10 A), the cells were discharged in series and were removed from the string when their terminal voltage reached 1.30 V, which corresponded to the "knee" of the discharge curves. At the high discharge currents (30 and 50 A), the cells were removed when their terminal voltage reached about 1.00 V, which corresponded to the knee of those discharge curves.

3. Results and Discussion

The average cell capacities and plateau voltages of each five-cell group at the various discharge currents and temperatures are given in Table 1. It is seen that plateau voltage generally varies directly with the ambient temperature as expected. However, the electrolyte concentration at the various discharge currents appears to have little effect on the plateau voltage. At 30°F and at discharge currents of 2 to 30 A, the plateau voltages are decreased by 0.01 to 0.05 V at the 50% concentration. On the other hand, at the 50-A discharge current, the plateau voltage is increased by 0.05 V at the 50%

Table 1. Average plateau voltages and cell capacities in each 5-cell group

Discharge current, A	KOH concentration, wt %	Plateau voltage, V, at indicated temperature			Cell capacity, A-h, at indicated temperature		
		30°F	75°F	100°F	30°F	75°F	100°F
2	50	1.47	1.53	1.55	32.5	47.0	47.5
	45	1.51	1.54	1.55	29.5	47.5	49.0
	40	1.51	1.54	1.55	36.0	50.0	47.5
10	50	1.41	1.50	1.51	20.0	42.0	48.0
	45	1.45	1.50	1.51	21.5	40.0	45.0
	40	1.45	1.50	1.51	24.0	44.0	47.0
30	50	1.30	1.43	1.42	21.0	26.0	25.0
	45	1.32	1.43	1.44	12.0	25.0	25.5
	40	1.34	1.43	1.44	11.0	26.0	24.5
50	50	1.20	1.35	1.38	14.5	26 0	29.0
	45	1.15	1.35	1.37	7.0	16.0	19.5
	40	1.15	1.35	1.38	7.5	17.0	19.0

concentration. During the development of the *Surveyor* battery (Ref. 1), electrolyte concentrations of 33 to 43% KOH were investigated. Those data showed that cell voltage and capacity were maximized at 40% KOH; however, discharge currents were relatively low, so the *Surveyor* data is not in conflict with the present data.

At low discharge currents and within the temperature range evaluated, it is seen in Table 1 that the electrolyte concentration has little effect on the cell capacity. However, at the high discharge currents, it is seen that cell capacity is increased at increased KOH concentration at all test temperatures. As might be expected, cell capacity tends to increase with temperature; however, the cell capacity for the 40% electrolyte tended to decrease slightly or stay relatively constant at temperatures between 75 and 100°F.

The results of this investigation indicate that the effect of electrolyte concentration on cell performance is a complex phenomenon. Cell design parameters such as the type of separator system, plate density, plate thickness, and quantity of electrolyte also play an important role in cell performance.

The results could, in part, be due to an internal heating effect. Since the conductivity varies inversely with the KOH concentrations, it is entirely possible that the internal heating of the cells produced the effects discussed here. Cell temperature was measured at the terminals during the discharge; however, the temperatures recorded are of little value because of the heat generated by current-resistance of the terminals and intercell connections. A study now in progress at Whittaker Corporation for Delco-Remy (Ref. 2) should help differentiate between the interaction of the heating and electrolyte concentration effects. In this study, individual plate or electrode performance is being evaluated as a function of electrolyte concentration and temperature.

In addition to the data presented here, cell shelf life is being investigated as a function of electrolyte concentration at temperatures from −60 to 120°F. Charge characteristics will be obtained on a second set of cells.

4. Conclusions

The data show that electrolyte concentration is an important consideration in the design of AgO–Zn cells and that the optimum electrolyte concentration is dependent on battery application. For example, if the requirement is one of high discharge current at low temperatures, a high electrolyte concentration should be used if the charging can be accomplished at room temperature.

References

1. Moses, A J., *Summary Report—Surveyor Main and Auxiliary Batteries.* Prepared under JPL Contract 952226. Hughes Aircraft Co., El Segundo, Calif., Oct. 1968.

2. Keralla, J. A., *Silver-Zinc Electrodes and Separator Research,* Technical Report AFAPL-TR-68715. Prepared under Air Force Contract AF 33(615)3487. Delco Remy Div., General Motors Corp., Anderson, Ind., Sept. 3, 1968.

B. Testing of Thermoelectric Generators,

P. Rouklove

1. Introduction

Thermoelectric generators and multi-element thermoelectric modules are being tested at JPL to: (1) provide a set of accurate performance data to allow thorough evaluation of the units, and (2) obtain the experience required for use of thermoelectric generators as power sources for future spacecraft. Seven thermoelectric generators have been, or are presently, under test. Figure 1 shows the JPL thermoelectric laboratory where four of the units are currently under test. Three units are being tested in an ambient condition, while the fourth is undergoing thermal-vacuum environmental tests in the special vacuum chamber.

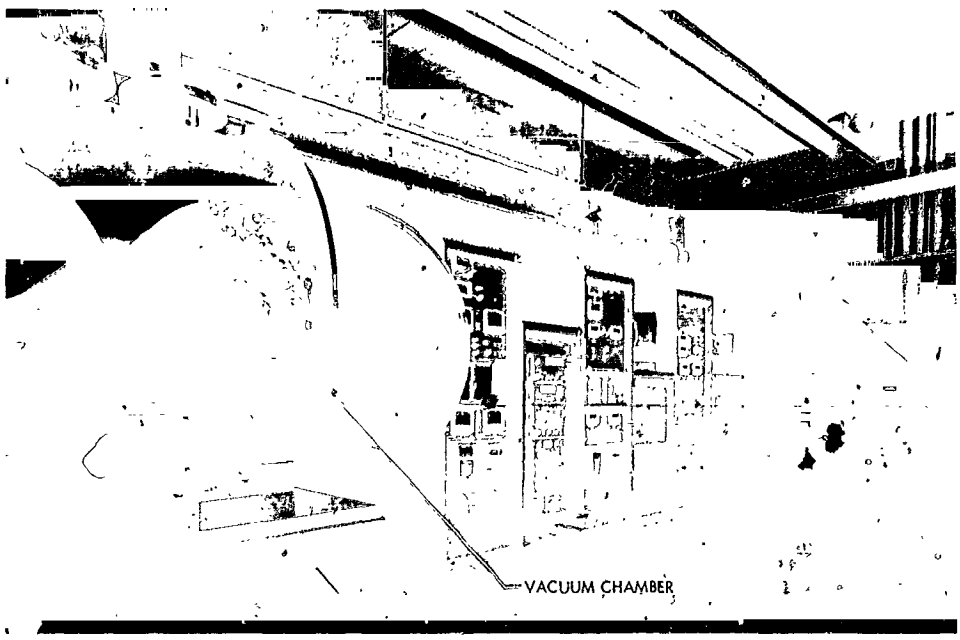

Fig. 1. Thermoelectric generator test facilities

One series of tests consists of extensive parametric evaluations of the generators at various predetermined values of power input and/or hot junction temperature. The power output and other values are recorded at each value of power input for selected values of voltage output. Another test consists of long-life term evaluation, generally at maximum power input and maximum power output, or a matched load condition. These tests are usually performed in ambient condition using the normal air convection cooling. Another series of tests is performed in a vacuum condition to simulate the environmental conditions that would be imposed on a thermoelectric generator during a space mission. During all tests, the generators are heated by radiant heat from a block being heated electrically, but simulating the mass and center of gravity of a radioisotope capsule.

2. Tests of the First SNAP 11 Generator, SN-2

a. Generator design. The SNAP 11 generator was designed as a possible power source for the *Surveyor* spacecraft. When technical difficulties precluded this usage, the program was redirected to further improve the performance of thermoelectric generators heated by radioisotope decay. Due to the short expected mission duration, the generator was to be fueled with curium-242, whose half life was judged sufficient for the 90 days of a lunar mission.

The design of the generator (shown in Fig. 2) includes provisions for excess isotope inventory, and a thermal mechanism to relieve the excessive thermal energy at the beginning of the mission. This mechanism consists of a thermal shutter that is activated by expansion of a column of NaK, the movement being transmitted through a bellows-and-lever arrangement to the hinged shutter mechanism. This arrangement can be regulated to release any amount of energy above the 550 W (thermal) that is calculated to be necessary for operation of the generator.

The heat source for the generator consists of a fuel capsule that, for purposes of testing, was replaced by an electrically heated block simulating the isotope capsule in size, mass, and center of gravity. The block contained eight sheathed electrical heaters equally distributed along the periphery. The capsule is located inside a metallic cavity, the outer periphery of which is covered with lead-tellaride (2P-2N) thermoelectric elements. These elements are pressed against the cavity wall by spring-loaded push rods and are insulated from the cavity by a thin insulating material with good thermal transmission properties.

The generator is surrounded by a second metallic container, in close thermal contact with the cold junction of the thermoelements, and is provided with fins to radiate the excess heat. The top of the cavity containing

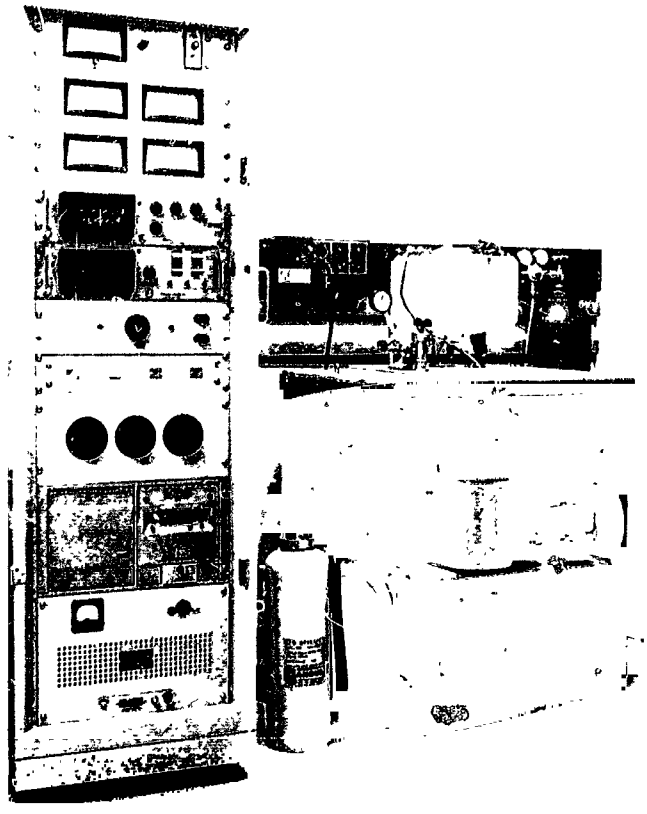

Fig. 2. SNAP 11 generator SN-2 in test

the heater block for the tests was covered by the thermal shutter. The intercavity spacing, hermetically enclosed, is packed with insulating material placed between the thermoelements and was filled with an inert gas to reduce the possible sublimation of the thermoelectric material at the operating temperatures. The SN-2 was provided with a valve to enable addition of the gas. During the tests, this valve was connected to a cylinder of the inert gas through a purifying system. (This arrangement proved to be very useful, since the generator was found to be leaking and gas had to be added to maintain proper pressure.) The nominal power output of the SN-2 generator is 30 W at 3.0 V, and the total generator weight is 30 lb.

b. Test equipment. The equipment used in the SN-2 tests (Fig. 2) was manually operated and consisted of a hot junction over-temperature control and the instrumentation used to read out the power input (volts and amperes) and the power output. A digital voltmeter and scanner were used to record the different instruments and thermocouple readouts. The generator load consisted of a variable resistor.

Power input was controlled by three Variacs preset for three modes of operation: (1) the initial period (lunar day), (2) the midterm operation (lunar night), and (3) the standby mode. Testing was performed in an ambient environment. The power input was adjusted to produce the hot junction temperatures and thermal conditions calculated to represent the various mission conditions. The thermal conditions were naturally heavily dependent upon the expected lunar environment (lunar day, +235°F; lunar night, −235°F).

A standby Variac was used in conjunction with the hot junction over-temperature protection circuit to reduce the power input by 30% in case of excessive heat. This arrangement avoided possible thermal shocks in case the guard circuit tripped the operating input level. To further avoid the possibility of a thermal shock due to loss of line voltage, a relay circuit was included to automatically select any of the three phases still operating. The line voltage was supplied through a voltage stabilizing circuit. All data were recorded on a digital printout on command.

c. Test results. The SN-2 generator was operated at JPL for approximately 3100 h, during which time some degradation in performance was observed. This was traced to an increase in the internal resistance of the generator, related primarily to a deficiency of the bonding of the thermoelectric elements to the "hot shoes." In spite of the fact that approximately 50% of the bonds were found to be deficient, the SN-2 generator was still operating well past the design time (90 days). By 3000 h, it had experienced a 20% decrease in its operating output.

During the tests, dc/dc power conversion system was tested in conjunction with the generator. The converter delivered a nominal voltage output of 28 V with an input of 3.0 V. Although the efficiency of the device was 87%, heavy losses were observed in the primary transmission line of 6 ft of 4/0 cable. Heavy current and voltage transients, resulting from magnetic effects in the power transmission lines, had to be eliminated by extra large capacitors. These losses drastically reduced the efficiency of the combination of the generator and the dc/dc converter.

3. Tests of the Second SNAP 11 Generator, QN-3

a. Generator design. Certain deficiencies observed in the SN-2 generator were corrected in the newer version of the SNAP 11 generator designated QN-3 (Fig. 3). This generator is hermetically sealed with the proper amount of gas. An improved control mechanism of the thermal

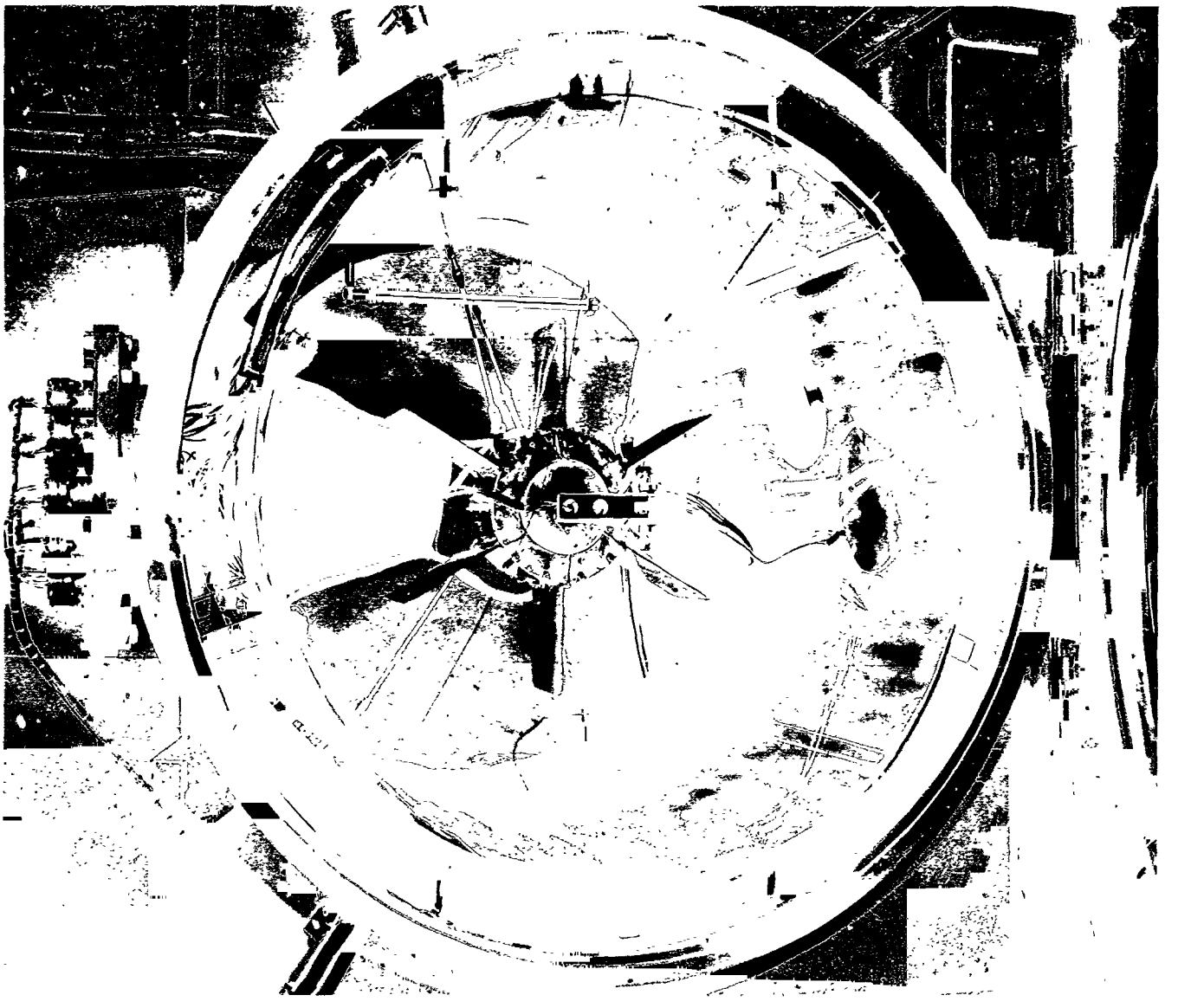

Fig. 3. SNAP 11 generator QN-3 during thermal-vacuum tests in vacuum chamber

shutter is included. The lead telluride thermoelements used are 2N-3P, which, although less efficient than the 2N–2P, are more stable, less fragile, and less prone to contamination. Also, the bond between the elements and the hot shoes is improved. The new 32-lb generator delivers slightly less than its nominal 30-W output.

b. Test equipment. The SN-2 generator tests indicated the need for accelerated testing and more reliable information; thus, the following improvements were made in the test equipment:

The manually operated Variacs were replaced by an automatic power input control built around a "data track" silicon-controlled rectifier. This arrangement allowed automatic control of the power input to within ±1 W, or control of the power input to maintain the hot junction temperature at a selected value to ±1°C. Parallel to that arrangement, a programming device provided the capability to vary the power input according to a pre-traced power/time curve with an accuracy of ±10°C or ±10 W. The resistive load was replaced with an automatically controlled solid-state load developed at JPL that provided the capability to maintain a selected voltage or current output to ±1 mV or ±1 mA.

The over-temperature circuit was further refined, and the open-circuit voltage and current reading circuits

were modified to record the data after a defined and constant period of time. The latter modifications were made since the previous readings, taken during an unstable operational period and estimated by the operator, did not provide the desired accuracy.

Data were recorded automatically on an hourly basis, 24 h/day, on data acquisition equipment with a capability for 300 programmed channels. All data were printed out automatically. This arrangement reduced the data-taking interval from 12 to 3 h, resulted in much more accurate data, and freed the technician, previously occupied full time with the operation of the generator, for other activities. The modified test equipment and the automatic data recording equipment are shown in Fig. 1. At present, the automatic data recording equipment is utilized to record the data from all the generators tested, as shown in Fig. 1.

The equipment was capable of fully automatic 24-h unattended operation. Visible and audible alarm systems were included to warn in case of operational deficiencies. To further reduce risks of thermal shocks due to power line failures, a battery bank was connected through a diode to cut-in automatically and instantaneously in case of reduction of the line voltage below a preset limit.

c. Test results

Ambient and thermal-vacuum testing. The generator was tested at JPL in air for 5600 h over a wide range of power input and power output. At the initial examination, it was observed that the generator was subjected to shock during transportation of above 10 *g* in the vertical direction. This may have resulted in the slight increase of the internal resistance with the corresponding decrease in power output that was observed but that was not indicated in the test data provided by the manufacturer. No power output degradation was observed during the tests.

Additional testing for approximately 4900 h was performed on the generator in a vacuum environment (Fig. 3). During this period, the generator was tested over a wide range of power input and output at shroud thermal conditions of 235°C and −235°F for three complete thermal cycles.

At the end of the third thermal cycle at a high shroud temperature, it was observed that the pressure of the inert gas within the generator was decreasing. This condition was attributed to high gas diffusion or leakage through the Viton "O" rings used in the hermetic seal of the generator. The thermal-vacuum tests were terminated when the inner generator pressure dropped from 14.8 to 10.8 psi.

Prior to delivery to JPL, the QN-3 generator had been operated by the contractor for approximately 2500 h. Comparison of the SN-2 and QN-3 test results indicated that the QN-3 generator did not present the power output degradation pattern observed with the SN-2. The SN-2 was observed to degrade along an exponential-type curve during the first 1000 h of operation, the curve slowly becoming asymptotic to a stable operational line. From initiation of the testing at JPL, the QN-3 generator operated in a straight-line pattern.

After the opening of the vacuum chamber, a heavy deposit (shown in Fig. 3) was observed on the walls of the chamber and in the vacuum system. The deposit, characterized as Au, Cd, Al, and Mg, was probably the result of the following processes: The Au evolved from the gold plating of the thermal shutter and the generator's top end; the Cd resulted from some of the braze materials used; and the Al and Mg evolved from some of the high-temperature cements used to affix the thermocouples and form the insulation layers separating the heating block from the inner can walls.

The deposit found in the vacuum system was of an organic nature (paraffin and other compounds) and could have evolved from the cover of some of the cables provided by the contractor that were used in the electrical interconnection between the generator and the test equipment. The results of the tests indicated that a thermoelectric generator could successfully operate for long periods of time in severe thermal environments.

Vibration and acceleration testing. The QN-3 was also subjected to vibration and acceleration tests in the Z (thrust) and Y spacecraft axes. During the tests, the generator was mounted 30 deg to the vertical to duplicate the possible position on the spacecraft.

The tests were performed with the generator heated with 570 W and electrically loaded to deliver approximately 15 W at 2.0 V. The tests consisted of acceleration up to 10 *g* static and vibration up to 18 *g* (peak), using both sinusoidal and complex wave forms. No high-intensity shock tests were performed. Some heater-shutter flapping was observed at excitation between 13 and 24 Hz, and the radiator fins vibrated.

Both tests were terminated as a result of heater block failures, once due to an internal short circuit of the sheathed heaters and once as a result of breakage of interconnecting wires within the heater block. Except for the heater block failures, the generator successfully passed the tests and appeared to operate properly, the power output being similar to that observed during some of the initial tests of the generator.

Future testing of the QN-3 generator will include long-term life testing at maximum power input and output compatible with the operating conditions of the generator.

4. Tests of SNAP 19 Generators

Two SNAP 19 generators, similar to those to be flown on the *Nimbus* spacecraft, were delivered to JPL for testing. One has 3P-2N lead telluride thermoelements, while the other has 2P–2N elements, but with improved bonding of the elements to the "hot shoes." Both generators, similar in outward appearance, were designed to deliver 30-W nominal power output.

The general internal construction of the SNAP 19 generators is similar to that of the SNAP 11 generators, although in detail they differ greatly. The major difference is that no thermal shutter is provided, since the generators are designed to operate with a long-half-life isotope. Both generators supplied to JPL were to be operated with electrical heaters for the tests.

One SNAP 19 generator (3P–2N) was first parametrically tested in ambient conditions at several values of power input and output for 2672 h. This generator has now completed 552 h of testing in the thermal-vacuum test chamber. The other SNAP 19 generator (2P–2N) was parametrically tested and is now being used in long-term life tests in ambient conditions to evaluate the new bonding technique. Its total operating time at JPL is 603 h. The test performance of the SNAP 19 generators will be discussed in a future issue of the SPS, Vol. III, as well as in JPL technical reports.

C. Power Conditioner for a Thermionic Diode Array, *G. I. Cardwell*

1. Introduction

A reactor thermionic power system requires a power conditioner to operate in conjunction with an array of thermionic diodes. Such a power conditioner has been developed to operate in an experimental test setup. Called the "kinetic experiment," a computer simulation of a reactor controls the heat energy to the array of real thermionic diodes functioning in a closed-loop test of the reactor thermionic power system. The power conditioner must be capable of switching the low-voltage high-current power generated by the diodes and must boost the voltage to a useful level. Ideally, the power conditioner should appear to be a dc transformer with a constant voltage setup ratio and predictable losses. The power conditioner should generate minimum voltage and/or current perturbations.

2. General Requirements

The general requirements for the power conditioner were specified as follows:

(1) *Input.* The input voltage shall vary from 5 to 1 Vdc as the input current varies from 0 to 600 A. Voltage and current spikes or ripple produced on the input bus by the power conditioner shall be minimal.

(2) *Output.* The output voltage of the power conditioner shall be unregulated and shall vary from 100 to 500 Vdc with the variations of input voltage.

(3) *Efficiency.* Though not the prime factor with the power conditioner, the efficiency shall be as high as possible within practical limits.

(4) *Reliability.* The breadboard shall have an expected life of 1000 h.

(5) *Protection.* Should the load impedance be lowered to a point where the input current exceeds 600 A, the power conditioner will shut off and will produce a signal to operate a mechanical switch to load the source.

3. System Design

Several types of "flyback" systems, bridge inverter systems, and center-tapped inverter systems were considered. The high amplitude of current necessitated the paralleling of power switches with any type of system used. These switches would have to be operated in a multiphase manner to reduce ripple and spikes, the number of phases depending upon the number of switches used.

The very low input voltage eliminated the bridge inverter systems, and the high setup ratios combined with low breakdown voltage switches eliminated the "flyback" systems. Thus, the only suitable system was the center-tapped inverter system. It appeared that five

center-tapped inverter systems switching in a five-phase sequence would handle the current. Each inverter should have a stepup ratio of 20:1. The rectified outputs of each inverter were placed in series to force current sharing and to present a total stepup ratio of 100:1. A clock-and-counter approach was chosen for the phase sequencing, because it appeared to be more accurate and more straightforward than the alternate method using a group of matched magnetic timers. Figure 4 shows the functional block diagram of the power conditioner.

4. Status of Development

At the present time, the total running logic, including the over-current and start/stop circuits, has been built and tested. One center-tapped inverter has been operated at 60% load, but specific performance data are not yet available.

D. Development of the Heat-Sterilizable Battery, *R. Lutwack*

1. JPL Contract 951296 With ESB, Inc.

This is a program for the development of AgO–Zn batteries that provide satisfactory performance after sterilization. Although the problems of (1) fabricating uniform cells, (2) decreasing capacity loss as a result of sterilization, (3) developing secondary cells, and (4) developing impact-resistant cells remain to be solved, considerable progress has been made.

Two batteries of six cells each (sealed after sterilization) were cycled at a depth of discharge of 60% nominal capacity. Failures occurred as early as 33 cycles, but the usual cycle life was 120 to 130; one cell reached 200 cycles. The failure mode was by Ag penetration through

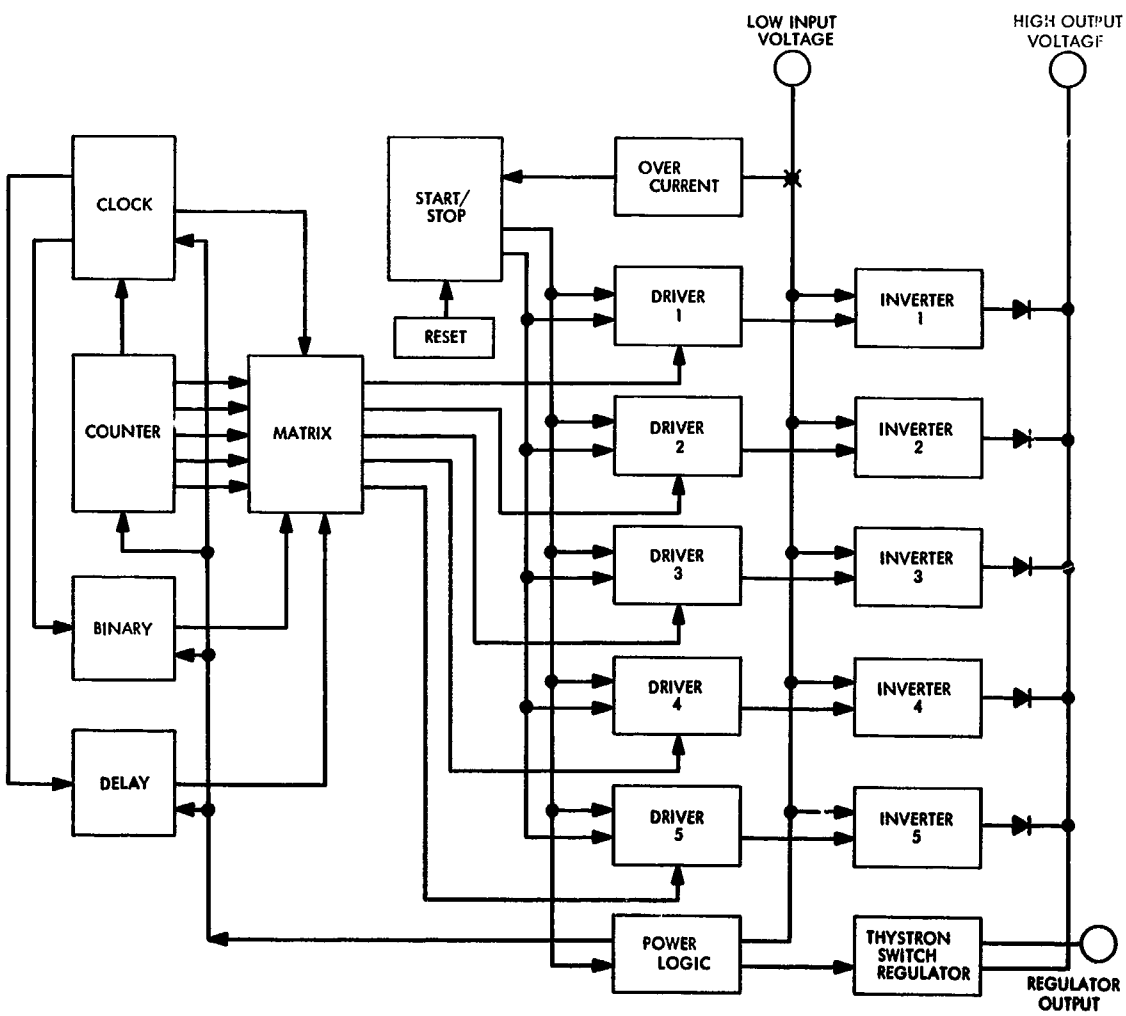

Fig. 4. Power conditioner block diagram

all of the separator layers, although there were indications of Zn shorting over the top of the separator to the lead wires of the Ag plates. It was concluded that additional layers of separator and a different Zn plate design are needed if the cycle life is to be extended. It was shown that the performance of a cell that is sterilized after being electrically cycled depends greatly on the state of charge. Prior to sterilization, the cell should be discharged so that no Zn metal remains and no HgO is formed. A procedure in which the discharges are made through successively larger resistances until an open-circuit voltage between 0.75 to 0.81 V is reached has been successful in reducing the capacity losses.

One of the causes of the non-uniformity of cells seems to be an attack on one of the plates by a component of the epoxy formulation used to seal the case. Modifications of the sealing technique are being explored in an effort to eliminate this problem. Electrochemical and design investigations continue in an effort to improve cell performance.

2. JPL Contract 951972 With Texas Instruments, Inc.

This is a research and development program for heat-sterilizable and impact-resistant Ni–Cd cells. From factorial design experiments in which the parameters were the separator, KOH concentration, percentage of pore fill, and heat sterilization, the following results were obtained from data for 35 cycles before sterilization and 30 cycles after sterilization:

(1) Capacities increased after sterilization an average of 33% for seven cells over 5 cycles.

(2) End-of-charge voltage increased after sterilization an average of 52 mV for seven cells over 5 cycles.

(3) Cell resistances were not significantly changed by sterilization.

(4) Capacity and the end-of-charge voltage after sterilization decreased with cycling.

(5) Pack tightness was shown to be an important design factor.

(6) Only one of the separator materials tested gave satisfactory performance.

This investigation of the effects of heat sterilization and the efforts to improve the cell design continue.

3. JPL Contract 952109 With the University of California at Berkeley

This is a research program to study the permeability characteristics of membranes as functions of different forces and includes a detailed theoretical application of the thermodynamics of the steady state to the transport across membranes and experimental determinations of the derived relationships. A practical method of transport-parameter evaluation from the basic flux equations of linear non-equilibrium thermodynamics has been outlined. A cell has been constructed for measuring osmosis, electro-osmosis, dialysis, transport number, membrane potential, streaming potential, and conductivity under uniform hydrodynamic conditions, using feedback mechanisms to keep solution concentrations constant despite the mass transfer that occurs. The cell is being tested to assure that it will conform to the design requirements.

E. Integrated Heat Pipe/Tubular Thermoelectric Module, *S. Bain*

1. Introduction

The use of an integrated heat pipe/tubular thermoelectric module as an energy conversion system for space application is currently under investigation at JPL. The heat pipe is used as a thermal coupling from the heat source to the hot junction surface of the thermoelectric module. Such a design makes the system flexible since the heat source can then be remote from the generator. The JPL test unit described herein employs an electrically heated source that simulates the isotope fuel that would normally be used in the final design. The satisfactory performance of the system thus far demonstrates that a heat pipe can be effectively used to thermally couple a heat source to a thermoelectric module. The information obtained in the tests described here will be useful in evaluating future devices employing heat pipe configurations.

2. Design

The integrated heat pipe/tubular thermoelectric module (Fig. 5), designed and fabricated by Westinghouse Astronuclear Laboratory (WANL), consists of a heat pipe and heater block, a tubular module, and a unidirectional radiator. The thermoelectric module and the aluminum unidirectional radiator are mounted on the condenser end of the heat pipe, while cartridge heaters fitted in nickel blocks are used on the evaporator end. All electrical instrumentation wires terminate in junction boxes on the test stand.

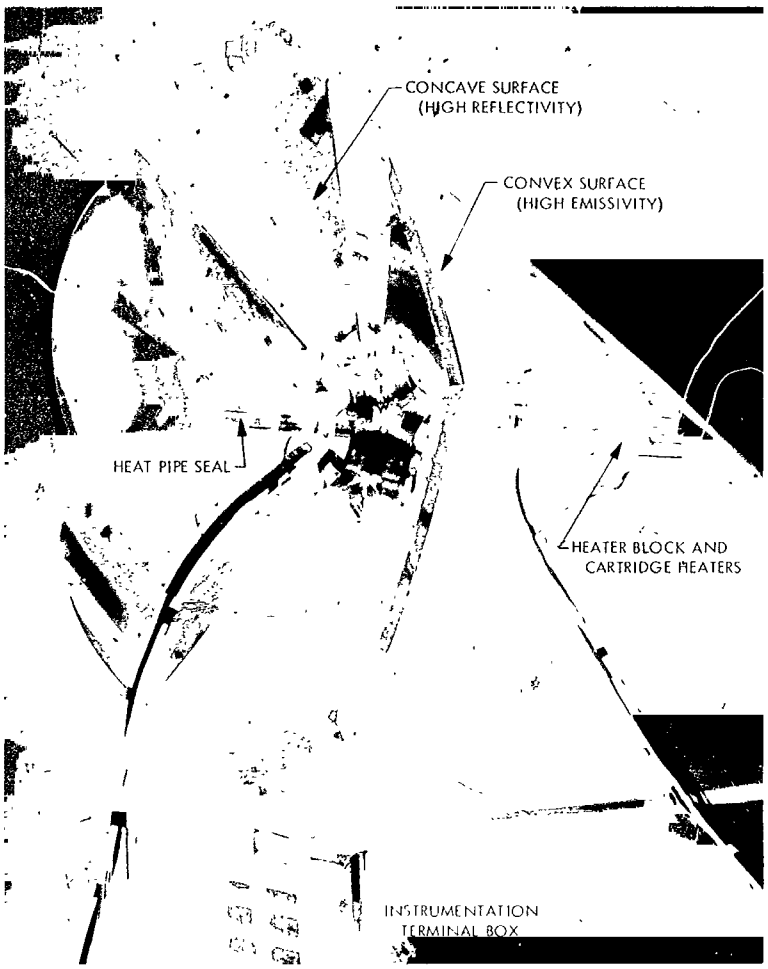

Fig. 5. Integrated heat pipe/tubular thermoelectric module

a. Tubular module. The heart of the generator is the tubular thermoelectric module developed for the Atomic Energy Commission by WANL. As shown in Fig. 6, the module has a 1.1-in. inner diameter, a 2.6-in. outer diameter, and a 7.2-in. active thermoelectric length.

b. Heat pipe and heater block. The total length of the 304 stainless-steel heat pipe is 18 in., with a 1-in. outer diameter. Approximately 37 cm^3 of sodium metal is used as the working fluid in the evaporator section. Heat is added to the sodium by conduction through the wall from nickel heater blocks. To assure good heat transfer between the evaporator and the nickel heater blocks, a layer of flame-sprayed copper is deposited on the evaporator end. Five layers of 60-mesh 304 stainless-steel screen are used as a wick and are held in place against the inner wall by a perforated stainless-steel sleeve.

The liquid sodium is transported in the vapor state throughout the condenser section and is returned to the evaporator by the stainless-steel wick. The heat is dissipated by the radiator attached to the outer wall of the thermoelectric module. Movement of the vapor arises from the natural pressure difference which results from the heat addition and removal. The cycle continues as the condensate is carried from the condenser end to the evaporator by the capillary action of the wick. Heat pipes are capable of a thermal conductance greater than that for any known homogeneous piece of metal. The heat pipe employed was capable of operating at a temperature of 1200°F with a heat transfer of 2800 W.

c. Unidirectional radiator. The radiator was fabricated from 6061 aluminum. Six finned sections are clamped on the outer periphery of the thermoelectric module. The hub of the assembled sections cover the condenser section

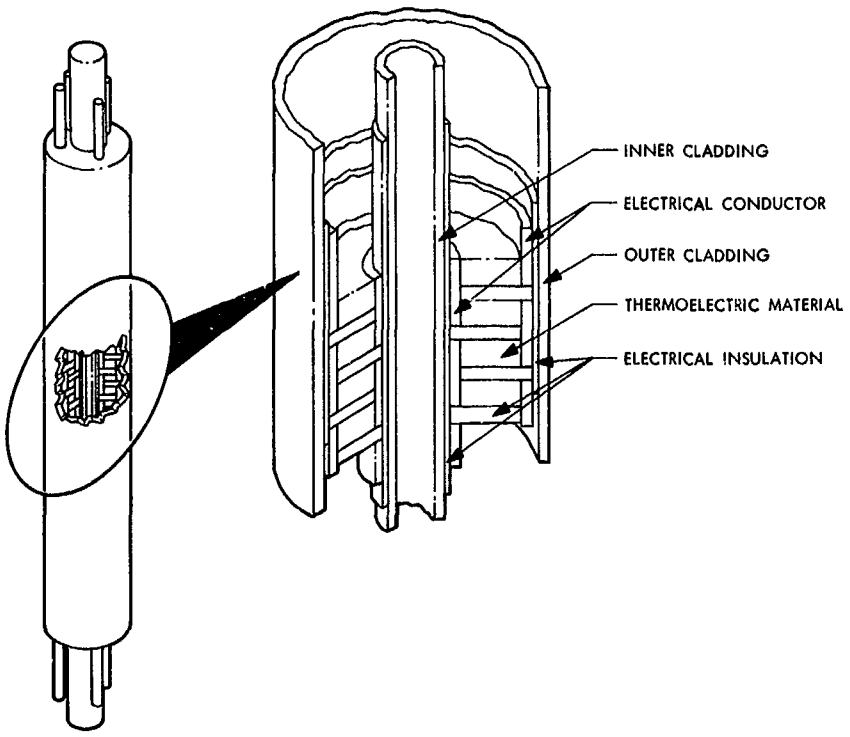

Fig. 6. Tubular module internal construction

of the system. To achieve a unidirectional radiator, the concave surface is highly polished for low emissivity, whereas the convex side is coated with a high-emissivity material. The nickel heater blocks clamped in place are shown in Fig. 5. The cartridge heaters are also exposed. In Fig. 5, the low-emissivity polished aluminum concave surface can be seen.

The radiator was designed to maintain the average outer clad temperature of the generator at approximately 200°C, with the average inner clad temperature of the generator at 535°C. The planar unidirectional radiator was not fully optimized for a particular space system, but serves merely to display a space concept in the employment of such a device.

3. Thermal Characteristics

To assure good heat transfer between the system interfaces, special consideration was given to specific areas, such as those between the heater blocks and the evaporator section of the heat pipe, the condenser section of the heat pipe and the module, and the module outer diameter and the radiator. The thermal impedance between the evaporator and the heater blocks was minimized by flame-spraying copper on the heat pipe and by machining the evaporator section to a precision fit with the heater block inner diameter. A boron nitride sleeve was inserted between the condenser section of the heat pipe and the module to accommodate the instrumentation needed to monitor the inner clad module temperatures. A high-temperature heat-transfer cement was placed between the interface of the radiator hub and the module outer surface to decrease the thermal impedance.

Verification tests were performed by WANL to determine the heat-transfer capabilities of the complete system and to assess the heat pipe performance under a module load. The temperature difference between the heat pipe and the module interface was less than 18°F. From the test data, the isothermal temperature distribution over the active length of the module was apparent.

4. WANL System Performance Testing

Prior to delivery of the completed system to JPL, the system was operated at WANL for 600 h at design conditions. Two thermal cycles were experienced, one after the first 433 h of operation at design temperatures, and the other after an additional 147 h. Figure 7 shows the data taken during the tests. The data taken before final shutdown prior to shipment are given in Table 2.

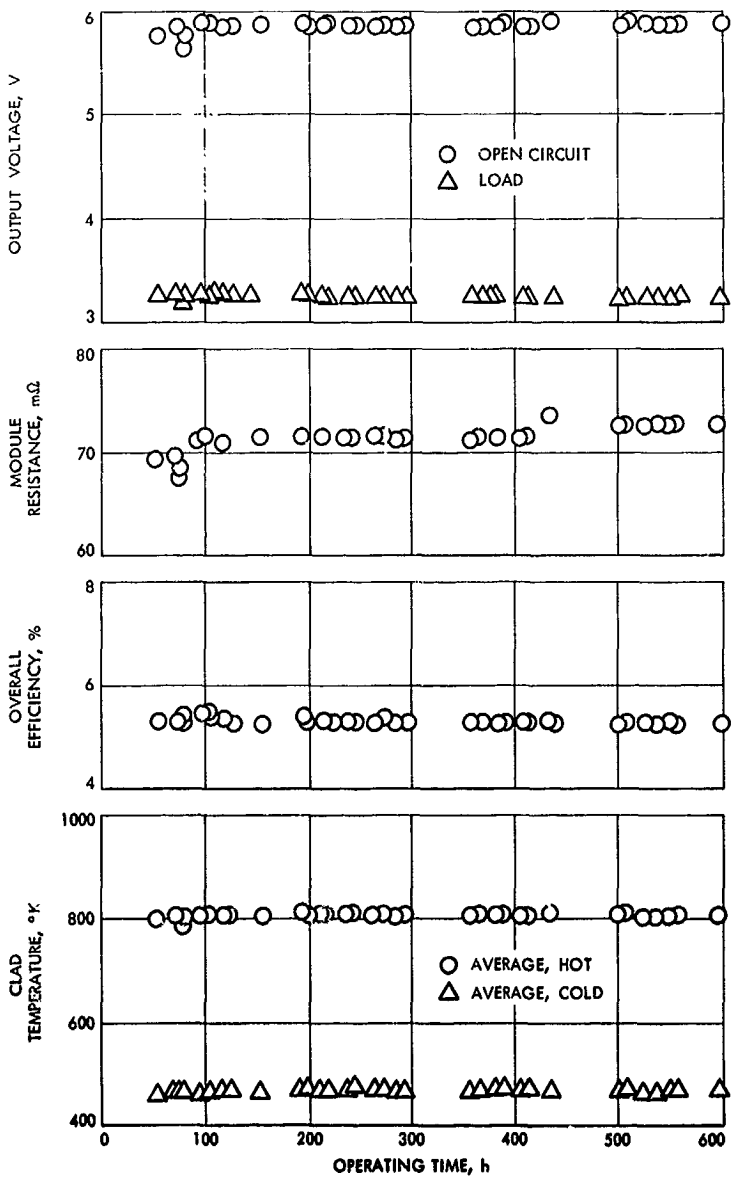

Fig. 7. WANL system performance data

Table 2. WANL and JPL initial system performance data

Characteristic	WANL initial data	JPL initial data
Average module inner clad temperature, °C	534	544
Average module outer clad temperature, °C	191	220
Open-circuit voltage, V	5.80	5.66
Load voltage, V	3.25	3.153
Load current, A	36.5	34.51
Power output, W	118.6	108.83
Power input, W	2140	2255
Overall efficiency, %	5.54	4.82

5. JPL System Performance Testing

a. Test instrumentation and techniques. In the continuation of the system performance testing at JPL, efforts were made to duplicate the test instrumentation and techniques used at WANL. The test apparatus was set up in the JPL environmental test facility. A matched-load condition was maintained at all times, except when open-circuit voltage data were taken. A maximum power input to the system was established at 2400 W, with the designed maximum inner clad temperature of 565°C (1050°F). Operation with 1050°F on the inner clad necessitated a limitation of 1100°F on the condenser

section of the heat pipe. After the 1100°F temperature was reached, power input was kept constant until temperatures stabilized along the heat pipe.

An adjustable load consisting of a group of fixed resistors was fabricated at WANL and used during the initial tests. A 0.162-Ω fixed resistor with taps at 0.027-Ω intervals and a 0.5- to 1.0-Ω trim was paralleled to the fixed section. This made the load adjustable from approximately 0.026 to 0.150 Ω. The total load consisted of the lead length from the output of the generator terminals to the fixed load. The measured resistance of 0.070 Ω was within 0.005 Ω of a matched-load condition when the module was operating at an average hot junction temperature of 535°C and an average cold junction temperature of 195°C.

The cartridge heaters were wired in a series–parallel configuration and operated from a 0- to 230-V supply dc source. An ac source was used at WANL. The primary circuit was controlled by an adjustable variable transformer (Variac). The electrical power input and increments as functions of time to attain the correct operating level are shown in Fig. 8.

Chromel-alumel thermocouples were used throughout the unit. Thermocouples of the sheathed type were attached along the module's inner and outer clad surfaces. All thermocouple readouts were per the National Bureau of Standards' millivolt temperature curves utilizing the correct cold junction compensation. An automatic data scanning system was used during the data acquisition. The outer clad of the tubular module was monitored with ten thermocouples; the inner clad, with four thermocouples; the radiator, with seven thermocouples; and the copper on the heat pipe, with three thermocouples. As many as possible of the original thermocouples were used to achieve a good comparison with WANL data.

Power input and output were measured with the data acquisition system. Precision shunts were used throughout to obtain direct readouts in millivolts. The open-circuit voltage was measured by reading across the voltage probes of the module when the load circuit was momentarily opened. An extremely fast readout instrument, a Hewlett-Packard Model 2401C integrating digital voltmeter, was used to obtain accurate measurements of the open-circuit voltage. The sampling period was kept small (approximately 0.1 s).

b. Test results. Operation was continuous for approximately 1367 h at a fixed power input of 2250 W. Plotted in Fig. 9 as functions of time are the efficiency, open- and closed-circuit voltages, power output, and module resistance. After the uninterrupted steady-state operation, a planned shutdown took place for a modification to the instrumentation. This shutdown constituted the third thermal cycle.

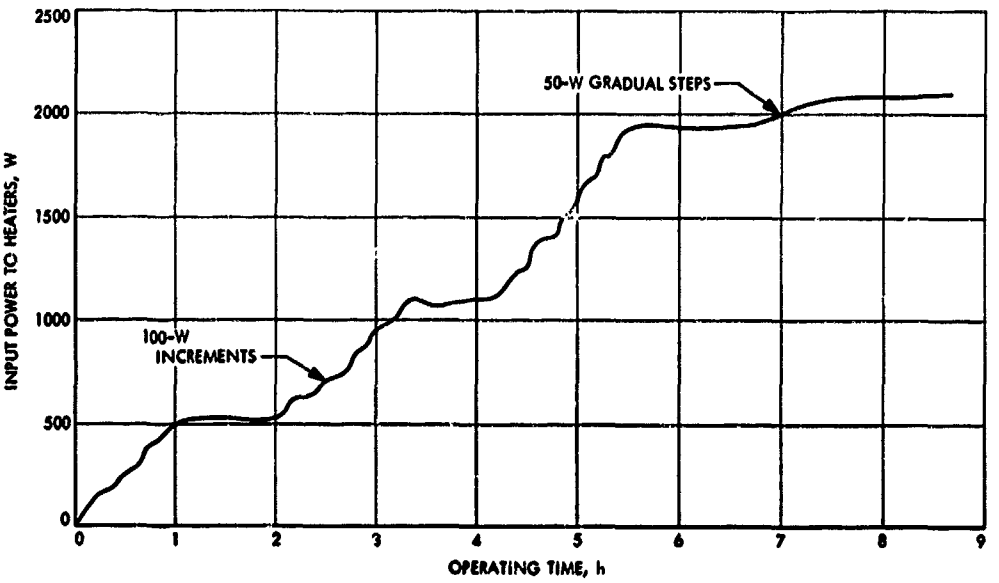

Fig. 8. Input power to heaters as a function of operating time: initial JPL data

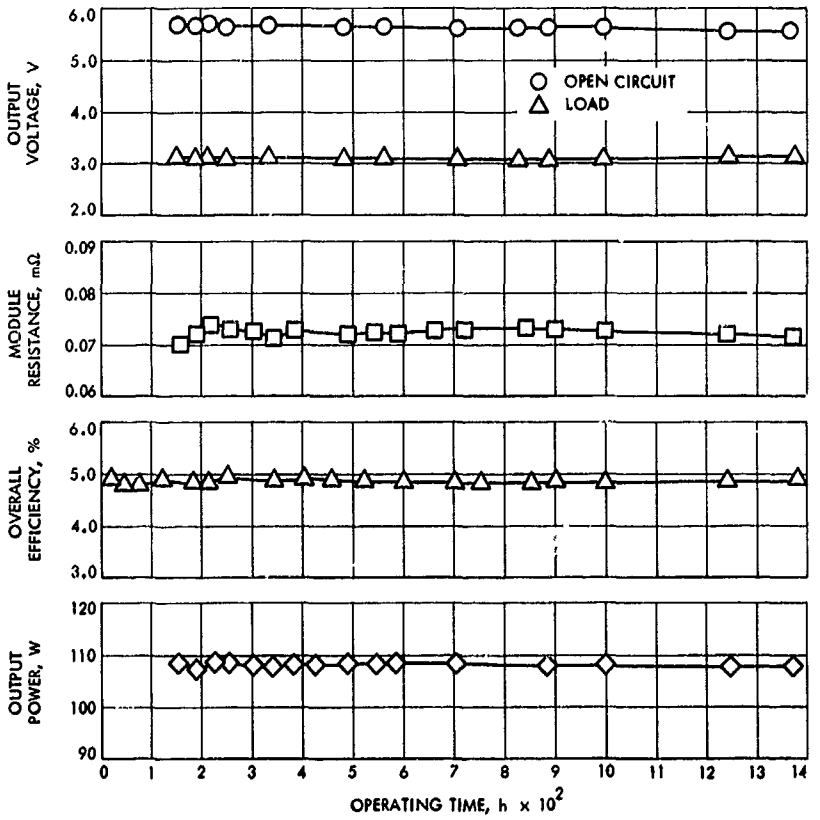

Fig. 9. JPL system performance data

System shutdown was initiated by cutting the electrical power to the heaters, thus permitting the system to cool down to ambient conditions. The data taken prior to shutdown are given in Table 2. These data represent the average data shown in the plotted points and are characteristic of the data produced on the first startup at JPL. The differences between the WANL anl JPL data were not explainable at the time of the JPL readings. The integrity of all instrumentation was verified. Resistance shunts between the module and the readout mechanism were eliminated as possible causes.

The second startup was interrupted with a power outage; at the time, the generator was producing 86.9 W for 2050-W input. A similar situation occurred during the third startup with a further reduction in performance; a power output of 82.0 W was noted for a power input of 2223 W. These shutdowns were the fourth and fifth thermal cycles on the generator. The power and instrumentation difficulties were solved and the testing was resumed.

A noticeable decrease in output was apparent on each restart. A decrease in module resistance was also detected. The temperature profile of the system remained essentially unchanged. The data were discussed in detail with WANL personnel in an attempt to determine the cause of the decrease in the observed performance.

The final shutdown of the generator took place with WANL personnel present. Prior to shutdown, the generator accumulated an additional 310 h under the following conditions:

Open-circuit voltage, V	4.04
Load voltage, V	2.39
Load current, A	26.7
Maximum power output, W	63.2
Power input, W	2360
Resistance, Ω	0.062

Diagnostic analysis is presently being conducted at WANL to determine the exact mechanism of failure.

VI. Guidance and Control Analysis and Integration

GUIDANCE AND CONTROL DIVISION

A. Support Equipment for a Strapdown Navigator, *R. E. Williamson*

The objectives of this effort are to provide a test van, data acquisition equipment, prime power, and system engineering for a strapdown electrostatic aerospace navigator (SEAN).

a. Van system. The test van has been procured and road tested with a mockup system installation that was comprised of consoles and lumped masses equivalent to a normal installation. These vibration and shock tests provided the information required for optimum location of the inertial measurement unit (IMU) in the van layout.

The vibration isolators for each of the cabinets have been procured and the design of the mounting cradles and baseplates established. The location of the SEAN system and its instrumentation is shown in Fig. 1.

b. Power subsystem. The uninterruptible power conversion unit has been procured and has been operated with dummy loads while being powered from the various optional power sources. Sources used included the 400- and 60-Hz laboratory powers, the 120-Vdc battery power, and the 400-Hz mobile engine–generator set power.

Design and fabrication of the power cabinet containing the power conversion unit and the three groups of nickel–cadmium batteries have been completed.

c. Data acquisition. The data acquisition system will provide the capabilities required to evaluate and troubleshoot the SEAN system. To meet these requirements, three means of data acquisition are to be used.

Digital recording system. A magnetic tape digital recording system will be provided to record computed system outputs (position, velocity, navigation time), total IMU data (gyro and velocity meter counts), and other required parameters. The system outputs recorded during flight tests will be used in conjunction with a recording of the range radar tracking of the aircraft to obtain system error plots. The total IMU data may be used for postflight analysis, such as separation of error sources, development of additional computer programs, improvement of gyro drift compensation schemes, and evaluation of the IMU and computer performance.

A complete recording system is being procured. The system manufacturer was provided with two flight-qualified digital magnetic tape recorders that were procured (Fig. 2). The design and fabrication of the recording system control unit, and the integration of the control

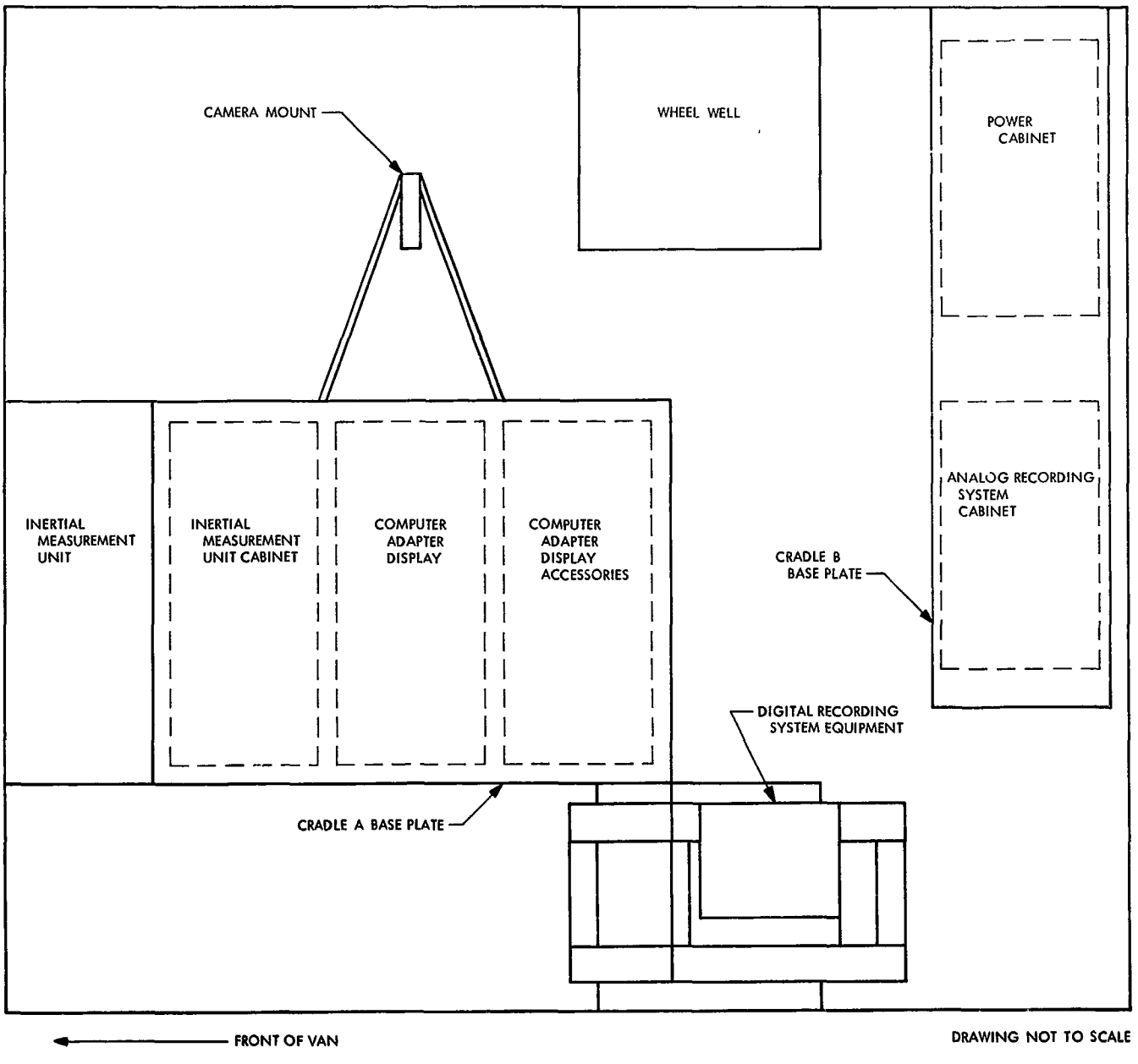

Fig. 1. SEAN van installation arrangement

Fig. 2. Digital magnetic tape recorder

unit with the Alert computer and the tape transports will be performed by the system manufacturer. Delivery of the complete system is expected in early December 1968.

Oscillographic recording system. An oscillographic recording system will be provided to monitor analog functions, such as gyro suspension G loading, IMU temperatures, gyro status, and power supply voltages. A Brush, Model Mark 848, 8-channel, thermal-writing recorder has been purchased as a versatile instrument to be used in monitoring the various IMU analog signals during laboratory tests, and for monitoring the gyro suspension circuits during flight tests. A second recorder, a Mid-Western, Model 603, 36-channel, optical-writing recorder, has been obtained from the JPL loan pool to monitor the additional IMU analog functions and the battery and power supply voltages.

Photo recorder. An instrumentation camera will be used to photographically record the computer-adapter display (CAD) output information (latitude, longitude, speed, azimuth, time). The camera is a 35-mm remotely controlled photorecorder designed for use in aircraft. It will be controlled by the SEAN Alert computer to photograph the display panel every 2 to 10 s to provide a continuous record of the flight test for at least 4 h. A lens has been procured, and the camera has been checked out optically and electrically.

d. Altimeter. A CPU-46/A altitude computer, Bendix Type 31101, has been procured to provide digitized altitude information. Integration of the altimeter with the SEAN computer-adapter display is planned for the first part of December 1968.

e. System integration support. System cables required for integration of the SEAN equipment into the van and flight test configuration are being procured. Approximately two-thirds of the required cables have been received with the balance due by the end of November. The SEAN system block and cabling diagrams have been updated and released. Detail schematics and signal descriptions have been prepared for those interfaces where equipments have not yet been integrated. Special interface tests are being run where necessary to define the interface characteristics.

VII. Spacecraft Control

GUIDANCE AND CONTROL DIVISION

A. Actuator Development for a Clustered Ion Engine Array, *J. D. Ferrera and G. S. Perkins*

1. Introduction

At the present time, there is a great deal of interest in solar-powered electric-propulsion systems suitable for interplanetary spacecraft applications. One such electric-propulsion application is a Jupiter flyby mission in 1975.[1] Another mission under study is an asteroid shot in 1974 using mercury electron-bombardment ion thrusters as an engineering experiment.

To prepare for these candidate flights, a breadboard system was designed and built in calendar year 1968 that incorporates the minimal features considered necessary for a deep space probe. All major components necessary for any solar-electric system are present. The portion of the system that will be enclosed in a vacuum chamber for system testing is shown in Fig. 1. The vacuum chamber end dome is 36 in. in diameter; the ion engines are 10 in. in diameter, 14 in. in length, and weigh 10 lb each. Each engine is gimballed to provide roll attitude control. The engine array is translated in the X and Y directions (in the test described, only one axis of translation is considered) to align the resultant thrust vector with the center of gravity of the spacecraft for pitch and yaw control.

[1]Barber, T. A., et al., *1975 Jupiter Flyby Mission Using a Solar Electric Propulsion Spacecraft*, Mar. 1, 1968 (JPL internal document).

2. Translation Actuator

The characteristics of the translation actuator (Fig. 2) are listed in Table 1. Two features are particularly noteworthy. One is the application of a harmonic drive gear train to obtain a very low value of backlash (<5 arc sec) and high output torsional stiffness. The other is the space compatibility of the flat-strap type of drive. Fatigue cracks that might develop in the strap are self-healing in space vacuum.

In this test the balls used in the roller bearings that support the moving platform on two 1-in.-diam rails are made of stainless steel. In a space vacuum application these balls could be made of a ceramic to eliminate the possibility of cold-welding. A rotary infinite-resolution potentiometer is used for position feedback. Where possible, similar metals are used to minimize thermal expansion problems. Thermistors are mounted inside the actuator to provide temperature information since the ion engines themselves are expected to reach temperatures as high as 500°F. Individual electrical lines are shielded to prevent electrical interference.

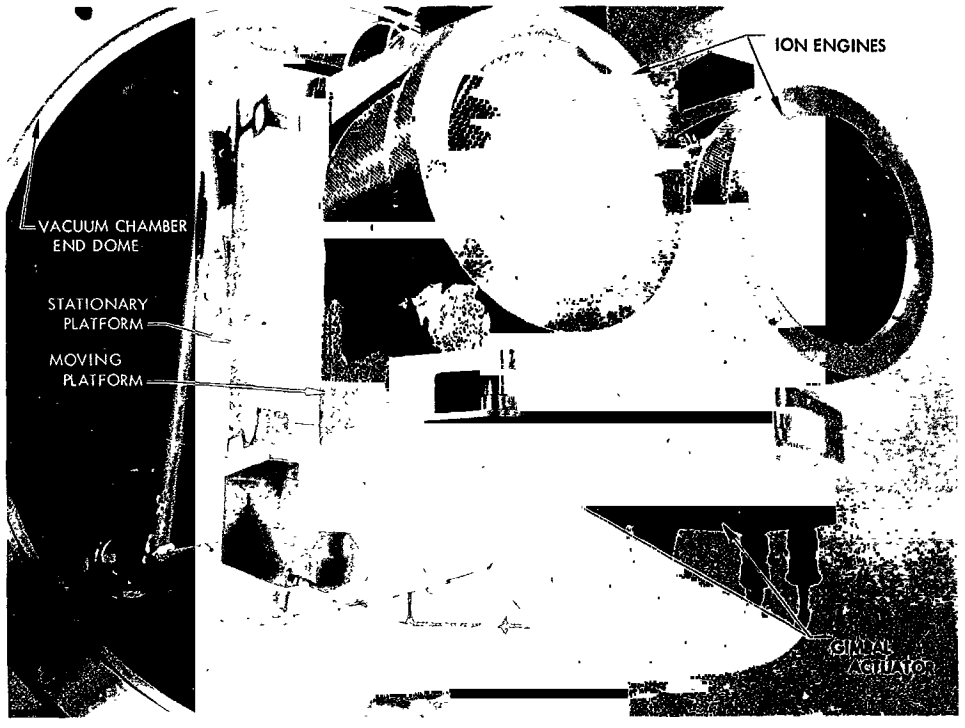

Fig. 1. Ion engine system

3. Gimbal Actuator

The characteristics of the gimbal actuator (Fig. 3) are also listed in Table 1. A unique feature of this actuator is the drive arrangement utilized to minimize backlash in order to obtain 20 arc sec per stepper motor step of output rotation. The linear motion of the saddle nut is transformed to rotary motion of the sector through two beryllium copper straps. The saddle nut is also pinched slightly prior to the machining of screw threads such that, in its assembled state, the screw threads are forced into contact with the lead screw threads. A solid rod connects the saddle nut to the pickoff arm. The pickoff for position feedback is a linear-variable differential transformer (LVDT). Thus, there is zero backlash between the actuator output shaft and the position pickoff.

The lead screw itself is a hollow aluminum shaft, hard-anodized after machining. Aluminum is used for the lead screw to maintain similar metals throughout to minimize thermal expansion problems.

The drive motors in both actuators are size 11, 90-deg permanent-magnet stepper motors. The actuator case is painted black and the intermediate shaft connecting the actuator to the ion engine is made of stainless steel to minimize heat transfer into the actuator.

Table 1. Actuator characteristics

Parameter	Translation actuator	Gimbal actuator
Output travel, in.	±3	–
Output travel, deg	–	±10
Nominal stepping rate, steps/s	100	50
Actuator slewing rate, in./s	0.25	–
Actuator slewing rate, mrad/s	–	5
Temperature range, °F	−50 to +275	−50 to +275
Test duration, h	1000	1000
Resolution, in./step	0.0025	–
Resolution, arc sec/step	–	20
Backlash, arc sec	< 5	0
Gear train ratio	2830:1	15708:1
Power required, W	7	7
Output torque at nominal rate, in.-lb	50	55
Weight, lb	7.25	4.3
Leak rate (90% nitrogen–10% helium), cm^3/h	< 0.005	< 0.005
Pickoff scale factor, V/deg	0.14	–
Pickoff scale factor, V/in.	–	12.55
Pickoff linearity, %	0.5	0.14 (full scale)
Excitation, Vdc	±24	24

4. Development Status and Projected Plans

The actuators for the breadboard system have been functionally tested and then assembled into the system

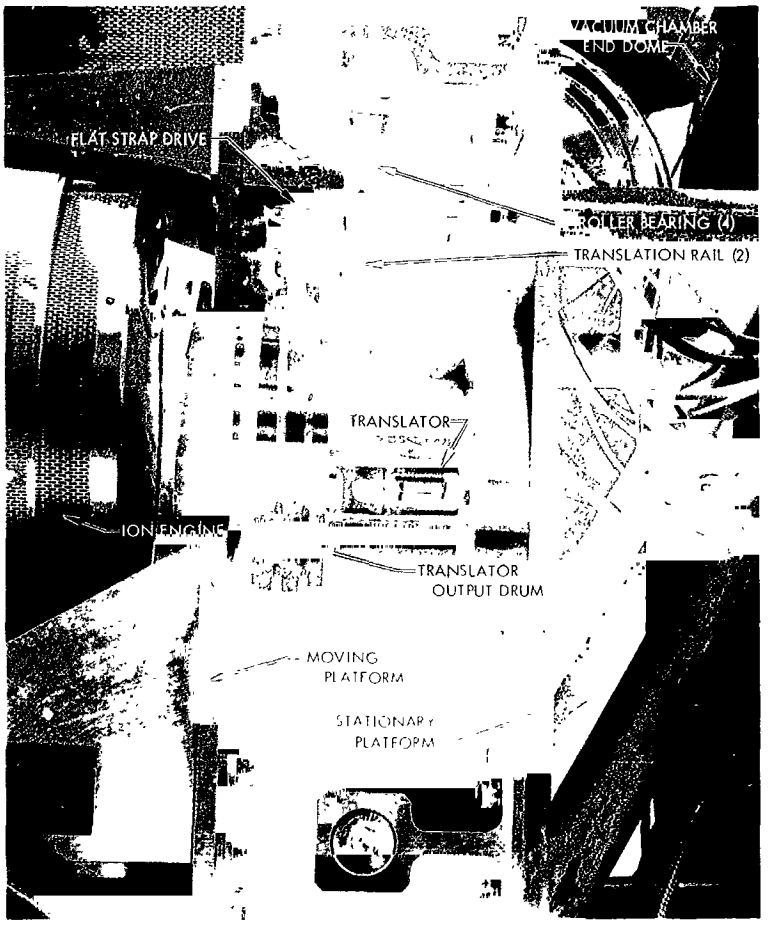

Fig. 2. Translator actuator

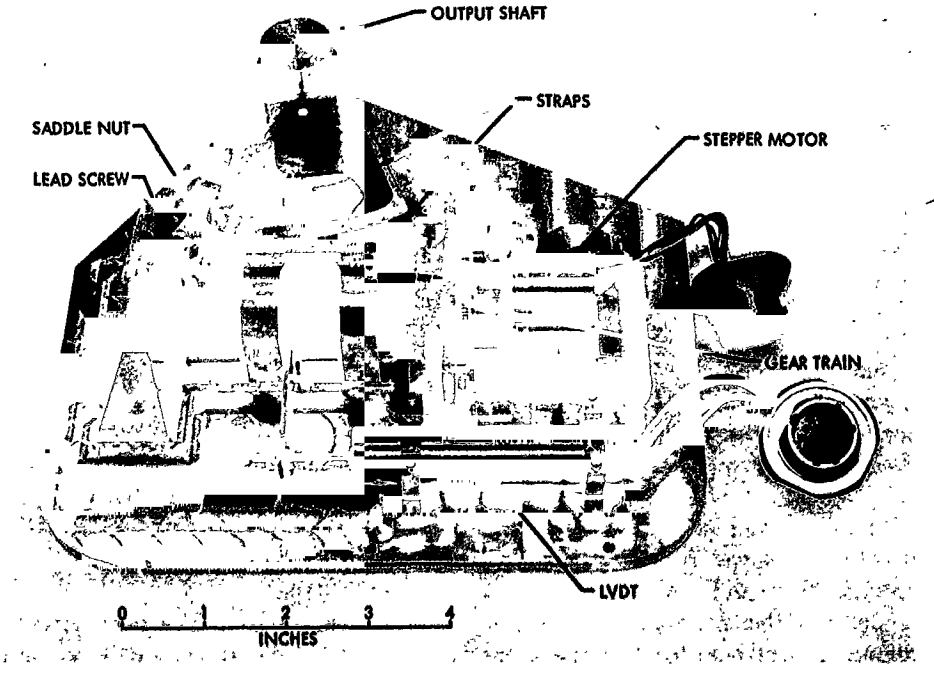

Fig. 3. Gimbal actuator

for a 1000-h test run in February 1969. No consideration was given in this breadboard system to weight reduction (flight requirement of less than 3 lb/actuator) or flight environmental requirements. These will be considered in the flight prototype system now being designed.

The prototype system, which will be ready for system test by the end of calendar year 1969, will be designed to provide two perpendicular directions of translation over a span in each direction of ±13 in. A closed-loop control system will also be provided for the new engine array.

B. Sterilizable Inertial Sensors: Gas Bearing Gyros, *P. J. Hand*

The objective of this task is to perfect a complete family of miniature inertial sensors that will be capable of withstanding both thermal and gas sterilization without either catastrophic failure or significant degradation of performance. Included in this family of inertial sensors are long-life gas bearing gyros of the single-axis, rate-integrating-type, subminiature ball bearing gyros, and high-performance linear accelerometers. All of these inertial sensors have potential applications in advanced planetary spacecraft, entry capsule attitude-control systems, and landed planetary missions.

The gas bearing gyroscopes selected for this development effort are the Honeywell, Inc., high-gain type GG159 and its low-gain, wide-angle counterpart, type GG334S. These gas bearing gyros do not have any bearing wearout conditions during operation and can, therefore, be considered for applications on any very long term planetary mission. The fabrication status and developmental history of both gyro types were covered in SPS 37-51, Vol. III, pp. 53–55.

The GG159E version is the culmination of a development program begun in 1962. This gyro has essentially met all of the design goals for performance through sterilization that were set forth at the beginning of the development effort. The program objective was to fabricate a gyro that would incorporate the major design goals of sterilization capability, high-g shock and vibration capability, low-power spin motor, and high-frequency fluid pump for the gimbal suspension system. Table 2 shows design characteristics of this unit.

The GG159E1 gyro (SN1) was fabricated and delivered to JPL in September 1968. Table 3 shows a comparison between the design goals and the actual performance of this instrument when subjected to thermal sterilization. The spin motor required 3.5 W of running power, which is well below the 4.0-W goal. In addition, the ability to build a gyro motor using approximately 2.5 W was demonstrated during the fabrication of one of the GG334S wide-angle gyros. Thus, further power reductions are a possibility if required. The decision to remain with a 3.5-W motor was based on obtaining the maximum motor torque margin consistent with the power design goal.

Table 2. Design characteristics of the GG159E gyroscope

Parameter	Value
Complete gyro unit[a]	
Diameter (excluding flange), in.	2.105
Length, in.	3.096
Weight, lb	0.997
Angular momentum, g-cm²/s	100,000
Input/output gain (at operating temperature)	155
Operating temperature, °F	
Nominal	115
Maximum limits	50 to 130
Output axis freedom, deg	+0.55, −0.56
Operating life (minimum)	
Hours	18,000
Start–stop cycles	10,000
Power of gimbal suspension pump (490 Hz, 100 V rms), W	0.6
Spin motor[b]	
Speed, rev/min	24,000
Power (26 V rms, 800 Hz, 2 phase), W	
Start	6.8
Run	3.5
Torque margin (to synchronize), V rms	21
Run-up time, s	15.7
Run-down time, s	56.7
Pickoff[c]	
Frequency, Hz	7200
Voltage, V rms	10.5
Sensitivity, mV/mrad	24.1
Null voltage, mV	1.2
Linearity, %	1.0
Torquer[d]	
Scale factor, deg/h/mA	356.1
Linearity, %	< 0.025
Stability, %	< 0.018
Maximum slew rate, deg/h	> 11,000
Temperature sensitivity (100 to 130°F), %	0.57
Heaters	
Warmup, Ω	265
Control, Ω	140
Sensor (at 115°F), Ω	780

[a]Single-axis, floated, rate-integrating, pumped-fluid gimbal suspension type.
[b]Hydrodynamic gas bearing type.
[c]Moving coil, air-core differential transformer type.
[d]Permanent magnet, moving coil type.

Table 3. Comparison of design and actual performance data of the GG159E gyroscope

Parameter	Design	Actual
FT, deg/h	±0.30	−0.158
MU_{SA}, deg/h/g	±0.50	1.54
MU_{IA}, deg/h/g	±0.46	0.414
Drift stability (rms)		
Run up to run up, deg/h	0.01	0.055
Cooldown to cooldown		
FT and RT, deg/h	0.03	0.09
MU_{SA} and MU_{IA}, deg/h/g	0.05	0.064
Random drift (1 σ), deg/h		
Output axis vertical	0.008	0.005
Input axis vertical	0.015	0.005
Elastic restraint, deg/h/mrad	±0.05	−0.042
Anisoelastic coefficient, deg/h/g^2	±0.05	0.02
Change of drift rates with sterilization (each cycle)		
Change in TSF, deg/h/mA	±4.0	0.065 (total)
Change in MU_{SA}, deg/h/g	±0.14	0.198 (max)
Change in MU_{IA}, deg/h/g	±0.14	0.202 (max)
Change in RT (total), deg/h	±0.07	0.095 (max)[a]
Change in elastic restraints, deg/h/mrad	±0.015	0.006 (max spread)

[a]Excludes first shift as not being typical.

One notable departure from the design goal was the optimum frequency of 490 Hz obtained for the piezoelectric, hydrostatic, gimbal suspension pump. (The design goal was 400 Hz.) The concept of the high-frequency pump was demonstrated in a previous JPL contract. The object of the current effort was to develop the necessary hardware to implement the new pump design into the GG159E gyro.

No less than seven variables are involved in the resonance of this piezoelectric pump. Among these are spacing, compliance, and mass of the piezo plates, as well as density and viscosity of the flotation fluid. The actual resonant frequency was of secondary importance to the application of this pump into the gyro; therefore, less effort was applied to obtain an exact 400-Hz resonant operation. (This is one area that can be improved in future development.) The pump assembly in the final device showed stable operation throughout the entire test program, including the sterilization cycling. Final test results on the pump were: power 0.6 W, frequency for best operation 490 Hz, and total operating time 585 h.

Prior to sterilization exposure, the gyro was subjected to an environmental test series consisting of: (1) shock, 200 g peak, 1.5-ms duration, 5 times in each axis; (2) vibration, 14-g rms random noise plus swept sinewave, 10 min in each axis; and (3) static acceleration, 14 g, 5 min in each axis. The shifts encountered in the critical parameters of reaction torques (RT), fixed torques (FT), mass unbalance on the input axis (MU_{IA}), and mass unbalance on the spin reference axis (MU_{SA}) are shown below.

Environment	ΔRT, deg/h	ΔFT, deg/h	ΔMU_{IA}, deg/h/g	ΔMU_{SA}, deg/h/g
Shock	−0.10	+0.10	+0.63	−0.24
Vibration	−0.02	−0.01	+0.02	+0.16
Acceleration	−0.05	−0.01	+0.06	+0.07

These results verify that, besides survival of the spin motor, the gyro performance was not significantly disturbed by such environments.

After completion of the above tests, the instrument was started into the thermal sterilization cycles. Each of the 6 cycles was 64 h in duration and a temperature of 135°C was sustained at the gyro. Performance data were taken before and after each thermal cycle. These data are presented in graphic form in Fig. 4, which displays, in a chronological sequence, the values of FT, MU_{SA}, and MU_{IA} as measured after the final assembly of the gyro and includes the sterilization cycling. The points designated as cooldown 1 through 5 represent a daily cooldown to room ambient (70°F) from the operating temperature of 115°F, and demonstrate the basic daily stability prior to sterilization. These data clearly show

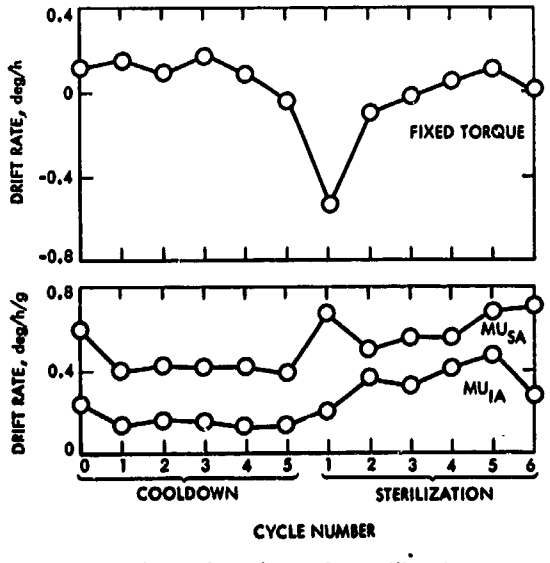

Fig. 4. Gyro drift through sterilization

that, except for the typical first cycle shift, the gyro performance is not significantly degraded by sterilization cycling.

In addition, other parameters, such as elastic restraints and motor performance, are shown in Table 4.

Except for the initial shift of fixed torque as a result of the first cycle (which has happened on other GG159 gyros in the past), no significant performance change will be noted in all of these test results. One item not listed in the table that is of particular interest is the torquer scale factor (TSF), which measured a change of less than 0.02% over the 6 cycles.

Two difficulties were encountered with the instrument after sterilization: an open spin motor rotation detector (SMRD) coil and decreased sensitivity in the eutectic balance capsule. Neither problem was directly related to the performance of the instrument as an inertial sensor. The SMRD winding is used during laboratory testing to observe spin-motor synchronism; it is not used in a flight application. The open SMRD coil was found to be inside the sealed gyro housing. Further investigation would entail a major disassembly of the gyro, and, since the SMRD coil was not related to the performance, the failure was not pursued further.

The balance capsule is used to make final vernier adjustments to the mass unbalance (MU) parameters without going into the gyro case. The capsule has already fulfilled its most important function at the time of initial MU trim; therefore, its decreased sensitivity did not warrant corrective action for this particular unit.

Additional effort to improve the sterilization capability of both the SMRD coil and the balance capsule would be in order for future production of this gyro.

The following conclusions can be drawn from the results of this development task:

(1) The GG159E gyro has successfully demonstrated compliance with the initial design goals of sterilization capability, high-g vibration and shock resistance, a low-power spin motor, and a high-frequency suspension pump.

(2) The GG159E is now a precision inertial sensor capable of application on any space mission requiring either sterilization capability, long life, or both.

(3) Corrective design actions needed to improve future units are very limited in scope and have no significant impact on the performance of the gyro. They are: improvement of the SMRD coil, improvement of the balance capsule, and adjustment of the suspension pump to operate on 400 Hz.

C. Ion Engine Thrust-Phase Attitude Control With Flexible Solar Arrays, *G. E. Fleischer*

1. Introduction

Increasing attention and detailed study have been given recently to the application of solar-array-powered electric-propulsion systems to specific missions to the Jovian planets.[2] Efforts to demonstrate the capability and practicality of an ion-engine-powered spacecraft has been mainly directed toward developing accurate dynamic

Table 4. Performance through sterilization

Parameter	Reference	Post 1	Post 2	Post 3	Post 4	Post 5	Post 6
Random drift (1σ) deg /h							
Output axis vertical	0.005	0.003	0.007	0.001	0.003	0.005	0.003
Input axis vertical	0.008	0.002	0.005	0.002	0.004	0.004	0.003
FT, deg/h	−0.022	−0.552	−0.092	−0.007	0.064	0.125	0.030
MU_{IA}, deg/h/g	0.130	0.208	0.370	0.333	0.423	0.485	0.287
MU_{SA}, deg/h/g	0.484	0.686	0.504	0.563	0.570	0.687	0.709
Elastic restraint, deg/h/mrad	−0.042	−0.046	−0.046	−0.048	−0.046	−0.047	−0.043
Run-up time, s	15.7	15.0	15.1	15.1	15.0	15.3	15.2
Run-down time, s	56.7	53.6	53.4	51.4	52.4	51.8	50.2
Power, W							
Start	6.82	6.50	6.80	6.60	6.70	6.40	6.40
Run	3.50	3.20	3.35	3.40	3.42	3.35	3.40

models of such a system and applying them to the spacecraft attitude-control design problem. This article describes some of the results obtained in assessing the dynamic interaction of large flexible solar panels with an attitude-control system based on ion engine thrust vector control.

2. System Dynamics Model

Attitude control of an electrically propelled craft, primarily due to the presence of very large and flexible solar cell arrays and the continuous force of the thrusters and solar winds, does not allow the use of the usual nitrogen gas or comparable mass-expulsion techniques since they result in unacceptably large system weights over the mission flight times involved. Thrust vector control must then be used for attitude control during powered phases. It becomes necessary, therefore, to provide for translation of the entire ion engine bank in two directions and to gimbal pairs of engines in order to achieve complete three-axis control. Several engine configurations are possible. For example, Fig. 5 shows a five-engine array designed for a Jupiter flyby mission (see *Footnote 2*).

In general, the control block diagram appears as shown in Fig. 6. Attitude error signals are supplied by the usual collection of celestial (sun and Canopus) sensors and transformed to engine coordinates. Control torques are applied to the craft as a consequence of the commanded engine translations and rotations. Stabilization and damping are achieved by feedback compensation about the engine control loop.

A major question has been the definition of an accurate mathematical model for the SPACECRAFT DYNAMICS block. Theoretically, this block must include the effects of what could be very flexible solar panels, or antennas, as well as the motion of relatively rigid but significantly

[2]Barber, T. A., et al., *1975 Jupiter Flyby Mission Using a Solar Electric Propulsion Spacecraft,* Mar. 1, 1968 (JPL internal document); also see Refs. 1 and 2.

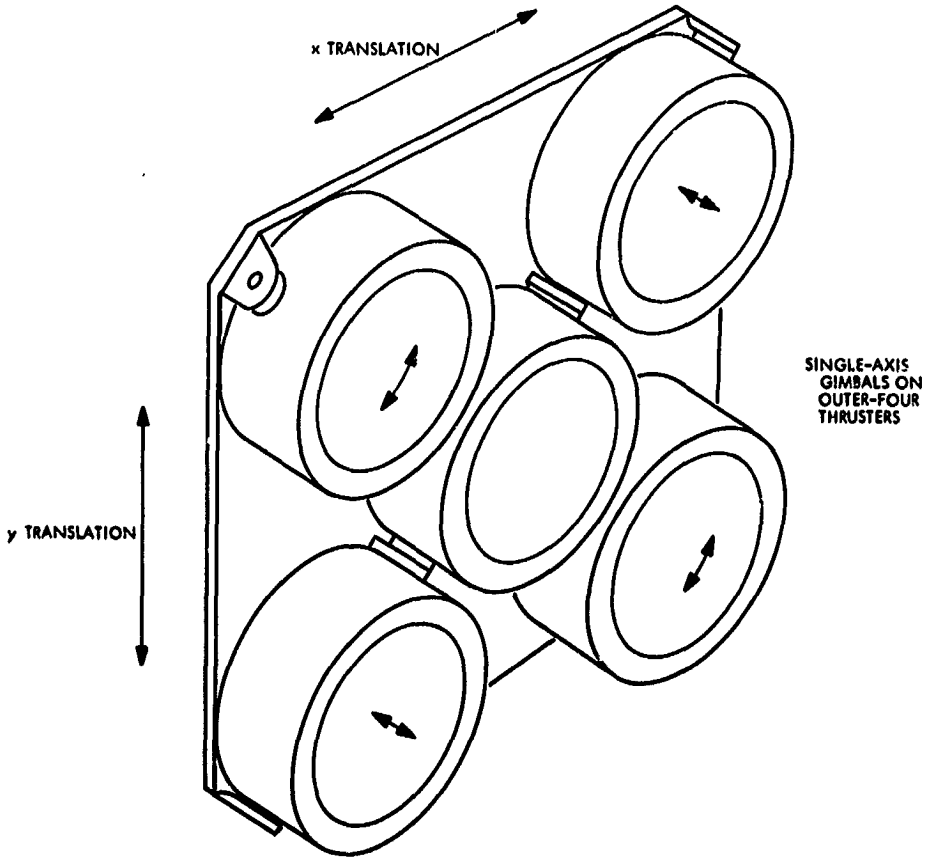

Fig. 5. Powered flight control using two-axis translation and third-axis gimballing

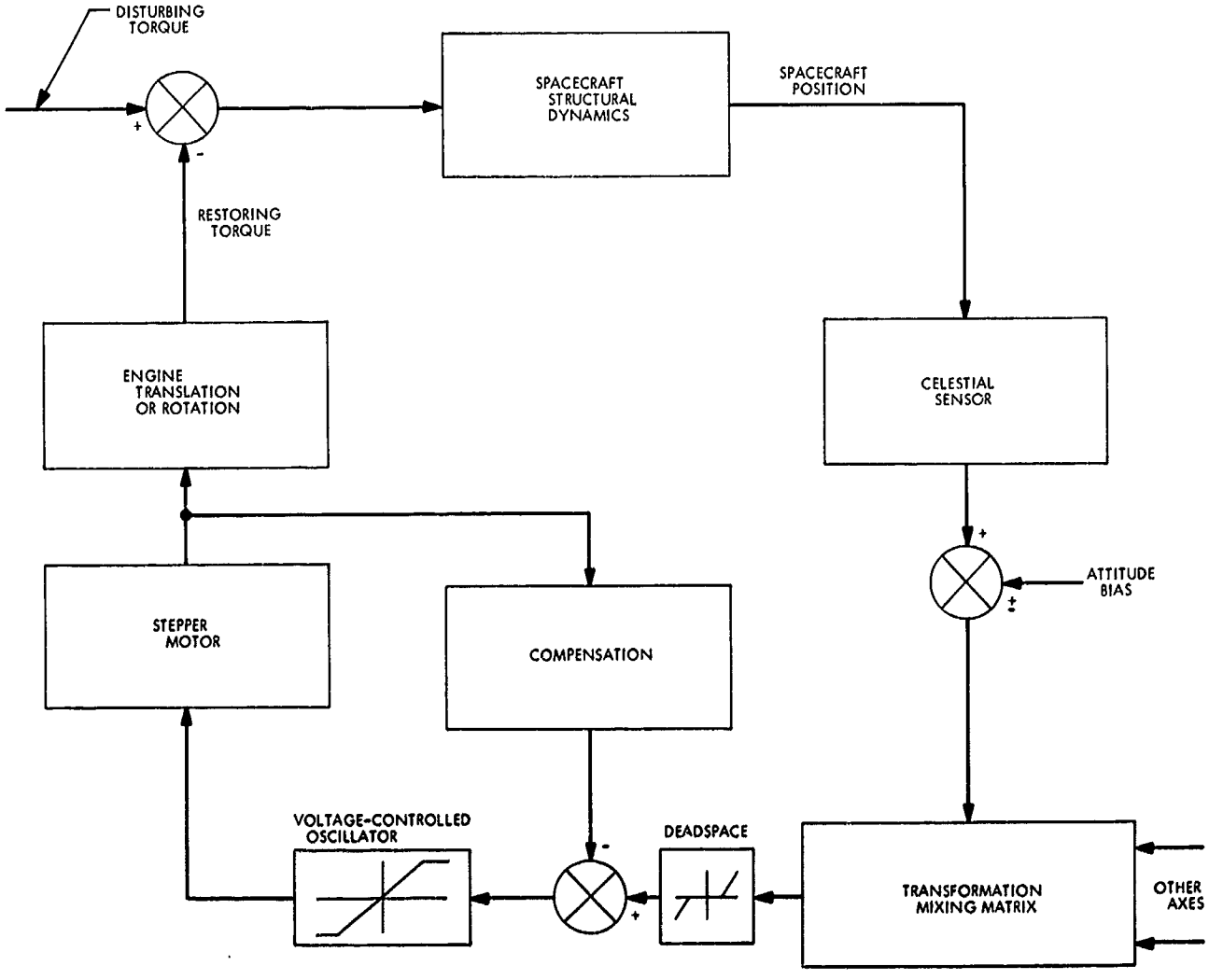

Fig. 6. Basic translation or gimbal control loop

large masses, such as an ion engine assembly or, perhaps, momentum wheels. Each of these interacts with the motions of the spacecraft's rigid central structure, or bus, which normally is the intended beneficiary of rotational control and therefore usually carries both the celestial and inertial sensors.

A great deal of experience and capability has been developed in the analysis of flexible structures using modal deformation coordinates, and they have long been efficiently applied to aircraft, missiles, and spacecraft as well. From the control standpoint, however, a *strictly* modal coordinate approach is not capable of accommodating rotors, nonlinear internal controls, discrete dampers, etc. At the same time, the opposite approach of modeling the system as a large collection of rigid bodies appears to be extremely cumbersome. Computer solutions to the resulting equations may be forced to include irrelevant high-frequency components, drastically increasing run times and therefore cost. Typically, the solution of large matrix equations are also required at each numerical integration step, aggravating even further the computational problem.

Recently, Likins[3] has developed in detail a "hybrid coordinate" approach to the vehicle control problem when flexible appendages are involved. It is based on the assumption that flexible portions of the craft may be accurately characterized by small, linearly elastic deformations and are therefore subject to modal analysis. Furthermore, if the flexible appendages are attached to a

[3]Likins, P. W., *Dynamics and Control of Flexible Space Vehicles*, Technical Report 32-1329. Jet Propulsion Laboratory, Pasadena, Calif. (in press); also see Refs. 3 and 4.

rigid base undergoing small motions or which has nearly constant angular velocity, normal modes of vibration can be shown to exist. Discrete coordinates are retained for describing the rigid base motion or the motion of other essentially rigid components, such as gimballed (or translated) engines, rotors, discrete dampers, and the like.

For example, if the spacecraft's rigid bus is assumed to experience a sufficiently small inertial angular velocity, so that second-degree terms and higher derivatives in this variable are negligible, the completely linearized matrix equation describing the flexible appendage becomes

$$M[E - \Sigma_E \Sigma_E^T M/\mathcal{M}]\ddot{q} + Kq = -M\Sigma_E[\ddot{X} + \ddot{e} - 2\dot{\tilde{e}}\dot{\theta} - (\tilde{e} + \tilde{R})\ddot{\theta}] + M\tilde{r}\Sigma_E\ddot{\theta} + \lambda \quad (1)$$

where

M = mass matrix of the flexible appendage ($3n \times 3n$) (n is the number of point masses used to model the appendage)

$\mathcal{M}$ = total vehicle mass (scalar)

q = column matrix of appendage deformation coordinates ($3n \times 1$)

K = appendage stiffness matrix ($3n \times 3n$)

X = inertial position of the system center of mass (3×1)

e = position of system mass center with respect to a point fixed in rigid base (bus), not including flexible appendage contributions (3×1)

R = location of appendage attachment point in rigid base (3×1)

$\tilde{r}, \tilde{R}$ = skew symmetric matrices locating masses in the flexible appendage ($3n \times 3n$, 3×3)

θ = inertial attitude of rigid base body (3×1)

E = identity matrix, any order

Σ_E = matrix $[E\ E\ E \cdots E]^T$, ($3n \times 3$)

λ = matrix of external forces applied to appendage ($3n \times 1$)

If in Eq. (1) the transformation $q = \Phi\eta$ is substituted followed by a premultiplication of the equation by Φ^T, where Φ is the matrix of eigenvectors of the homogeneous equation, the coefficient matrices of $\eta, \ddot{\eta}$ are diagonalized. Suitable normalization of the eigenvectors and insertion of a diagonal structural damping matrix results in

$$\ddot{\eta} + 2\zeta\omega\dot{\eta} + \omega^2\eta = -\Phi^T M\{[-\Sigma_E(\tilde{e} + \tilde{R}) - \tilde{r}\Sigma_E]\ddot{\theta} + \Sigma_E(\ddot{X} + \ddot{e} - 2\dot{\tilde{e}}\dot{\theta})\} + \Phi^T\lambda \quad (2)$$

Equation (2) may then be reduced in dimension (η's are uncoupled) to eliminate those modal coordinates η with unwanted high frequencies.

In addition to appendage Eq. (2), a vector equation of motion can be written for the entire vehicle from the basic relation $\mathbf{T} = \dot{\mathbf{H}}$, which in matrix form becomes

$$[I - I_w E]\ddot{\theta} + (\tilde{R}\Sigma_E^T + \Sigma_E^T\tilde{r})M\Phi\ddot{\eta} + A_E\ddot{u}_E = T - \tau - \tilde{\theta}I_w\dot{\phi} \quad (3)$$

where

I = total undeformed vehicle inertia matrix (3×3)

I_w = spin-axis moment of inertia for each of 3 identical momentum wheels whose spin axes are parallel to the reference axes (scalar)

$\tau = [\tau_1\tau_2\tau_3]^T$, momentum wheel applied torques

$\dot{\phi} = [\dot{\phi}_1\dot{\phi}_2\dot{\phi}_3]^T$, momentum wheel spin rates

T = matrix of torques applied to rigid base (3×1)

For the case of the solar-powered electric-propulsion spacecraft considered here, Eq. (3) includes acceleration (or torque) coupling of the ion engine bank, so that

$$u_E = [y_T x_T \alpha_1 \alpha_2 \alpha_3 \alpha_4]^T$$

where

x_T, y_T = translation coordinates of the engine assembly

$\alpha_1, \alpha_2, \alpha_3, \alpha_4$ = gimbal angles of each ion engine

and A_E is, in general, a matrix (3×6 in this case) of time varying coefficients that reflect the location and geometry of the ion engine assembly with respect to a point fixed in the bus.

To complete the system equations of motion, relations can be written for each of the engine coordinates and each momentum wheel spin coordinate. In matrix form,

they appear as

$$A_{EE}\ddot{u}_E + A_E^T\ddot{\theta} + A_\eta\Sigma_E^T M\,\Phi\,\ddot{\eta} = \lambda_E(\dot{\theta}, \dot{u}_E, u_E, \ddot{X}, F_i) \tag{4}$$

and

$$I_w[\ddot{\phi} + \ddot{\theta}] = \tau \tag{5}$$

where

A_{EE}, A_η = constant coefficient matrices

λ_E = matrix of velocity and position dependent forcing functions or applied forces (6×1)

F_i = thrust applied by the ion engines (scalars)

The relation $\ddot{X} = F/\mathcal{M}$, where F is the matrix of force components applied to the vehicle (3×1), is also useful.

3. Applications

The hybrid coordinate dynamic model described here has been programmed for attitude-control system simulations on both the IBM 7094 digital computer (using the DSL/90 language) and an Electronic Associates 231-R analog computer. Several solar-array configurations and high-gain antenna structures, designed for a specific flyby mission to Jupiter, Saturn, Uranus, and Neptune, have been analyzed in terms of modal coordinates. Results from these simulations will be presented in subsequent articles.

References

1. *Solar Powered Electric Propulsion Spacecraft Study*, JPL Contract 951144, Hughes Aircraft Co., Culver City, Calif., Dec. 1965.
2. *Solar Powered Electric Propulsion Program Summary Report*, JPL Contract 951144, Hughes Aircraft C.., Culver City, Calif., Dec. 1966.
3. Likins, P. W., and Wirsching, P. H., "Use of Synthetic Modes in Hybrid Coordinated Dynamic Analysis, *AIAA J.*, Vol. 6, pp. 1867–1872, 1968.
4. Likins, P. W., and Gale, A. H., "Analysis of Interactions Between Attitude Control Systems and Flexible Appendages," paper presented at the 19th International Astronautical Congress, Oct. 14–19, 1968.

VIII. Guidance and Control Research

GUIDANCE AND CONTROL DIVISION

A. Preignition Characteristics of Cesium Thermionic Diodes, *K. Shimada*

1. Introduction

Preignition volt–ampere curves of thermionic diodes operating in an electron-rich emission mode exhibit two clearly distinguishable features in their apparent saturation regions characterized by two different rates of current increase as a function of applied voltage. The region having a slower rate is designated the "Schottky-like" region; the remainder is designated the "avalanche" region (SPS 37-51, Vol. III, pp. 82–86). It is apparent that the rate is determined by how the space–charge sheath controls the current flow through the diode since the diode current is space–charge-limited. In the Schottky-like region, the space–charge sheath is controlled mainly by those ions produced at the emitter by surface ionization; in the avalanche region, by those ions produced in the volume. This article describes results obtained from a fixed-gap cesium diode, as well as from a variable-gap cesium diode.

2. Fixed-Gap Diode

A fixed-gap cesium diode, built by Electro-Optical Systems (EOS), Pasadena, California, and designated SN-107, was described in SPS 37-51, Vol. III. The diode has two rhenium plane-parallel electrodes. The electrode area is 2.00 cm² and the interelectrode gap is 0.0115 cm.

The diode was operated in an electron-rich emission condition for which two regions of preignition characteristics were clearly discernible. The emitter temperatures were 1284, 1386, 1495, and 1598°K, and the cesium temperatures were between 473–553°K. Typical preignition characteristics were reported previously, and their analyses are given in this article.

The normalized current I/I_0, i.e., the ratio between the measured current I and the apparent saturation current I_0, varies exponentially with applied voltage V. The empirical relationship between I/I_0 and V is

$$I/I_0 = \exp[k_1(V - V_1)] + \exp[k_2(V - V_2)] \qquad (1)$$

where k_1, k_2, V_1, and V_2 are constants for a given volt–ampere curve taken at fixed emitter temperature T_E and cesium-reservoir temperature T_{Cs}. The first and second exponential terms in Eq. (1) represent the current in the Schottky-like and avalanche regions, respectively. The two regions are clearly distinguishable on I–V curves plotted in semilog form. In general, $k_1 < k_2$, $V_1 \simeq 0$, $V_2 > 0$.

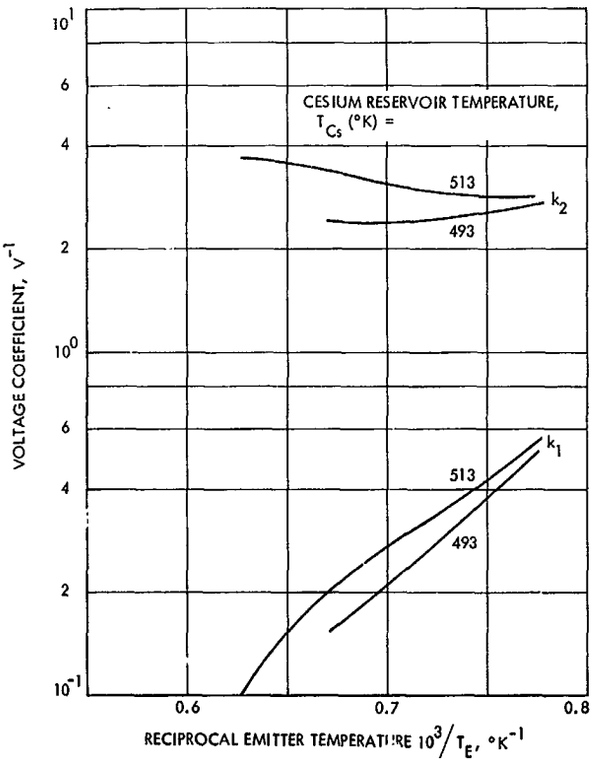

Fig. 1. Voltage coefficients vs $10^3/T_E$ for a fixed-gap diode

Figure 1 shows the dependence of k_1 and k_2 on reciprocal emitter temperature $10^3/T_E$ in the thermionic diode SN-107. The voltage coefficient k_1 increases exponentially with $10^3/T_E$, but varies only slightly with T_{Cs}. The coefficient k_2, on the other hand, does not vary significantly with $10^3/T_E$. These results were in good agreement with those obtained from a similar thermionic converter (SPS 37-50, Vol. III, pp. 122–125), except that k_2 in this converter was smaller than k_1 in the previous one for the same T_{Cs}. This difference was attributed to different interelectrode gaps d which were 0.0115 cm in the SN-107 and 0.0712 cm in the previous diode.

3. Variable-Gap Diode

To further investigate the effect of d on the preignition characteristics, experiments were carried out using a guard-ringed variable-gap thermionic energy converter. This converter was recently acquired from the Marine Engineering Laboratory, Annapolis, Maryland, as surplus equipment. It was fabricated by Thermo-Electron Co., Waltham, Mass., for the Navy, and is equipped with see-through sapphire windows to allow optical measurements of d and T_E. The converter has a separate electron-gun section that is continuously pumped by an appendage pump and, hence, is operable under normal atmosphere. The collector guard ring can eliminate the side-wall effects which ordinarily exist in hardware-type converters such as the SN-107. The variable-gap arrangement allows an effective separation between the surface and volume effects on preignition characteristics.

Volt–ampere curves were obtained for this diode in an electron-rich, unignited mode. The observed T_E ranged between 1173–1373°K, and the T_{Cs} between 453–533°K. The true T_E were not determined because of unknown temperature corrections required for the sapphire window, but the corrections should not have exceeded +10 and −0°K.

The d was varied between zero and 0.142 cm by means of three micrometer screws pushing against the collector flange. A zero-gap condition was established by noting a collector–emitter short; the parallelism was achieved during zero gap adjustments. Subsequently, d was set by the calibrated micrometer screws and occasionally cross-checked against the cathetometer readings. In order to correct for thermal expansions, the zero-gap condition was reestablished whenever the T_E was changed. The maximum error in d would be ±0.005 cm considering electrode surface roughness, parallelism, and measurement errors.

A visual observation of the d during diode operation confirmed that the avalanche region was associated with the *anode-glow* mode of the diode, which was originally found by E. O. Johnson (Ref. 1) and later identified in a thermionic converter by N. S. Rasor (Ref. 2). An increase in the diode current in the avalanche region of the volt–ampere curve was accompanied by increased intensity of a faint orange glow at the collector. The glow appeared to be localized near the center of the collector, and no glow was observed on the guard ring.

Preignition volt–ampere curves obtained at T_E=1173°K and T_{Cs}=533°K are shown in Fig. 2 for various interelectrode gaps ranging between 0.023–0.142 cm. The Schottky-like and avalanche regions are again clearly distinguishable because of the two different slopes of the I–V curve. Note also that the curves in the Schottky-like regions are parallel to one another in Fig. 2 for all values of d. In Fig. 3, where the current is normalized, the Schottky-like regions for six curves at various d converge to a single line. Therefore, the rate of current increase in this region is mainly controlled by the emitter surface; this conclusion is consistent with the previous findings

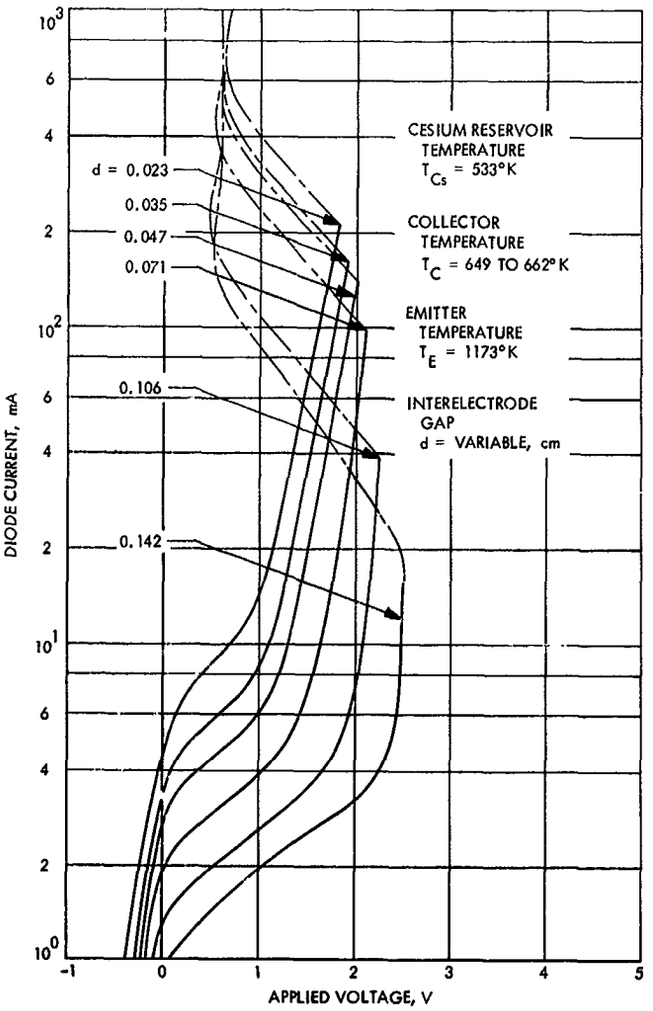

Fig. 2. Preignition volt–ampere curves for a variable-gap diode: semilog plot

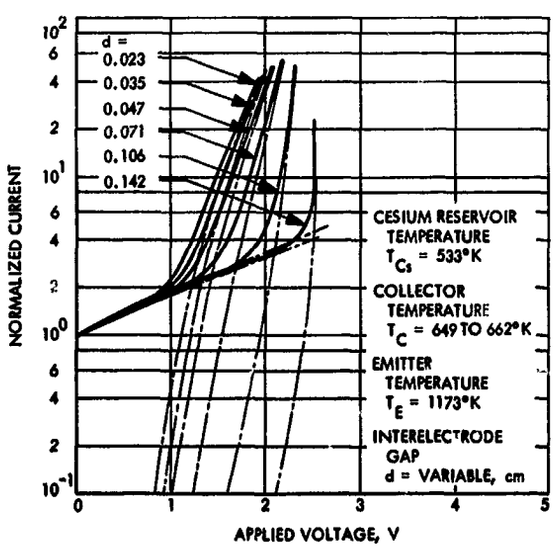

Fig. 3. Preignition volt–ampere curves for a variable-gap diode: normalized plot

with a fixed-gap diode. The voltage coefficients k_1 and k_2 are in agreement with the previous results obtained at similar T_E, T_{Cs}, and d. As is shown in Fig. 3, the rate of current increase becomes larger as d becomes larger; thus k_2 increases with d. This dependence is not surprising since volume ionization takes place in the avalanche region, and, therefore, k_2 may well depend on the product of pressure × distance. Further analysis is required to establish an exact functional relationship.

An additional feature of the *I–V* characteristics that was not found in a fixed-gap diode was revealed with the variable-gap diode. Previously, each observed normalized current could be decomposed into *two* exponential components in that it could be graphically represented as a sum of *two* straight lines in a semilog plot. On the other hand, each current for the variable-gap diode could be graphically resolved into the sum of *one* straight and *one* curved chain line (Fig. 3). Observing that the curved chain line converges toward the current in the avalanche region, and that the bend occurs at a voltage where the transition in normalized current occurs from the avalanche region to the Schottky-like region, one might conclude that a *third* term describing the current at the transition must be added to fit the observed current. The origin of this extra term is not clear at this time.

The electron-rich condition (ion-richness ratio $\beta < 1$) was verified by examining the relationship between the apparent saturation current I_0 and the inverse interelectrode distance $1/d$ (Ref. 3). The linear relationship shown in Fig. 4 confirms that, as expected, the diode was operating in an electron-rich mode.

References

1. Malter, L., Johnson, E. O., and Webster, W. M., "Studies of Externally Heated Hot Cathode Arcs: Part I. Modes of Discharge," *RCA Rev.*, Vol. 12, pp. 415–435, Sept. 1951.
2. Bullis, R. H., *et al.*, "The Plasma Physics of Thermionic Converters," *IEEE Report on the Thermionic Conversion Specialist Conference*, pp. 9–30, Oct. 1965.
3. Warner, C., and Hansen, L. K., "Transport Effects in the Electron-Rich Unignited Mode of Cesium Diodes," *J. Appl. Phys*, Vol. 38, No. 2, pp. 491–500, Feb. 1967.

B. Barrier Heights of Blocking Contacts to Vacuum-Cleaved Photoconducting CdS in the Conducting State, *R. J. Stirn*

1. Introduction

Potential barriers formed at a metal-semiconductor junction when the metal contact has a work function ϕ_m greater than the electron affinity E_A of the semiconductor

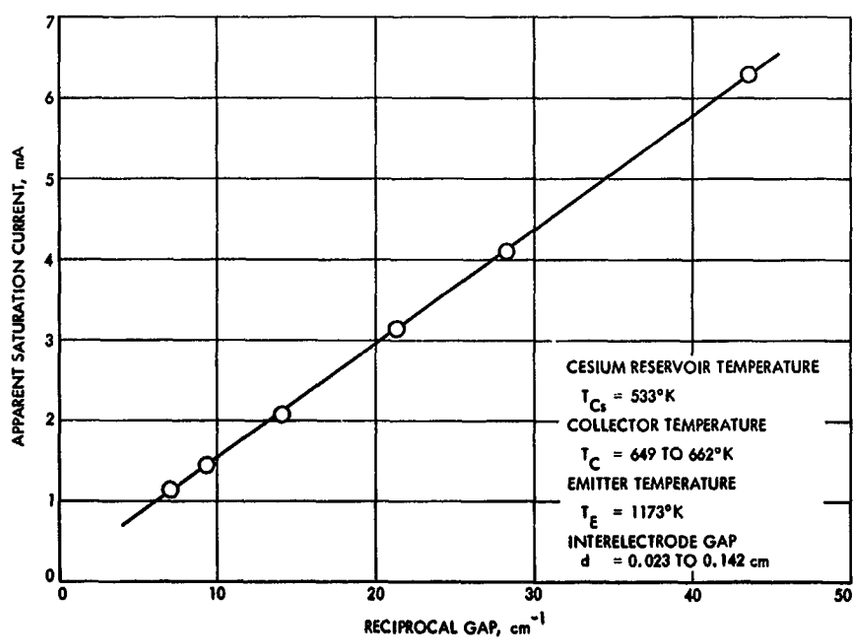

Fig. 4. Apparent saturation current vs reciprocal gap

have been measured for nonphotoconducting cadmium sulfide (CdS) by the techniques of photoresponse and differential capacitance (Ref. 1). The results have been summarized in SPS 37-53, Vol. III, pp. 68–71. Generally, the barrier heights depended upon the metal and ranged from 0.85 eV for Pt and 0.79 eV for Au to 0.36 eV for Cu, with no dependence upon temperature. Also, some preliminary results were given of barrier height measurements on photoconducting CdS, which is of much higher resistivity because of the presence of Cd vacancies. These results showed barrier height values of approximately 0.50 eV at room temperature with little dependence on the metal work function, and, more importantly, showed that the values depended strongly on temperature and photocurrent (light intensity). The results were obtained from an analysis of stationary high-field domains in the range of negative differential conductivity (Ref. 2). It is the purpose of this article to present a summary of the theory, the experimental techniques involved, and additional data.

2. Theory of Stationary High-Field Domains

Under certain conditions of doping and light excitation, field-enhanced excitation of hole traps in photoconducting CdS leads to increasing recombination (i.e., decreasing electron concentration) with increasing applied voltage (field quenching). In this negative differential conductivity (NDC) regime, high-field domains form at the cathode and either remain fixed in place while growing in size or propagate through the crystal in times on the order of seconds per millimeter. The photocurrent saturates or oscillates at low frequency, respectively, in these two cases. The Gunn effect in n-type GaAs is an example of NDC for which the decreasing conductivity with increasing field is caused by increasing scattering of electrons into a subsidiary conduction band having lower carrier mobility. In this case, the domains move with the velocity of sound and the current oscillates in the radio-frequency range.

Although the domains in CdS have many interesting features in relation to bulk properties, it is the fact that one can obtain information about n_c, the carrier concentration near the metal cathode–semiconductor interface, that will be utilized in this investigation. The value of n_c is then related to the barrier height ϕ_B at the cathode by the relation

$$n_c = N_c \exp\left(\frac{-\phi_B}{kT}\right) \tag{1}$$

where N_c is the effective density of states for the semiconductor, k is the Boltzmann constant, and T is the absolute temperature.

Above a critical voltage, the current saturates and the high-field domain can be observed by means in *Subsection 3*. We now wish to examine why the domain forms, i.e., how there can be two regions in the crystal having different field strengths. It has been shown (Ref. 3) that step-like solutions can exist as stationary solutions of Poisson's equation

$$\frac{dE}{dx} = \frac{q}{\epsilon \epsilon_0}(n + n_t - p - p_t) \tag{2}$$

and the transport equation

$$\frac{dn}{dx} = \frac{q}{kT}\left(nE - \frac{j}{q\mu}\right), \tag{3}$$

where

E = electric field

q = electronic charge

j = current density

μ = electron mobility

ϵ_0 = permittivity of free space

ϵ = static dielectric constant

n, p = free electron and hole densities, respectively

n_t, p_t = ionized electron and hole trap densities, respectively

It is required that the electron density have a range that decreases more rapidly than linearly with increasing field (because of enhanced hole excitation), and that the amount of diffusion current be negligible ($dn/dx \approx 0$). The actual solutions to Eqs. (2) and (3) require an appropriate reaction kinetic equation describing the trapping and releasing of carriers, i.e., dn/dt, and necessitate computer computation after reasonable values are assumed for the reaction kinetic coefficients. It will suffice for our purposes to examine the problem graphically.

Image forces at the cathode are neglected for the present so that Eqs. (2) and (3) form an autonomous system, i.e., do not contain the distance from the cathode explicitly. The solutions can, therefore, be discussed in

terms of their projection in the n–E plane at any convenient value of x. Since it is experimentally observed that the electric field is constant in the crystal (except at the domain edge and very close to the contact where image forces are no longer negligible), and that diffusion current is negligible, one introduces auxiliary functions $n_1(E)$, for which $dE/dx \equiv 0$, and $n_2(E)$, for which $dn/dx \equiv 0$ (Fig. 5).

The function $n_2(E)$, representing the condition of diffusion neutrality, is obtained from Eq. (3): $n \alpha (1/E)$. When plotted in logarithmic coordinates, as in Fig. 5, the curve $n_2(E)$ is linear with a negative slope of unity. The charge neutrality curve $n_1(E)$, drawn arbitrarily in Fig. 5, shows a constant carrier density (n_i = bulk low-field concentration) up to a certain field strength, above which there is a range where n decreases more rapidly than linearly, so that (as we will show) two singular points, or homogeneous solutions, can exist. It has been shown experimentally that the shape of $n_1(E)$ in Fig. 5 does conform to physical reality for the type of crystals used in this investigation (Ref. 4).

Examination of Eqs. (2) and (3) (with the left-hand sides identically equal to zero) for $n > n_1(E)$ and $n > n_2(E)$ shows that the slope $dn/dE \equiv (dn/dx)/(dE/dx)$ is positive. This fact is symbolized in Fig. 5 by the short arrow in the first quadrant. Similar reasoning leads to the directions shown for the other three short arrows depending on whether n is above or below $n_1(E)$ and $n_2(E)$ at the value of electric field desired. These arrows "point toward" increasing x. Therefore, for the simple case of a nearly homogeneous field at low voltages before current saturation, and under the assumption of a blocking contact at the cathode, the solution curve must lie close to the drift-current curve $n_2(E)$ (since diffusion in CdS is small compared to drift), and must pass from the region of the n–E plane in Fig. 5 near n_c (the carrier concentration at the cathode), to the region for which $E = E_I$ (the homogeneous field) and $n = n_i$, while x varies from the

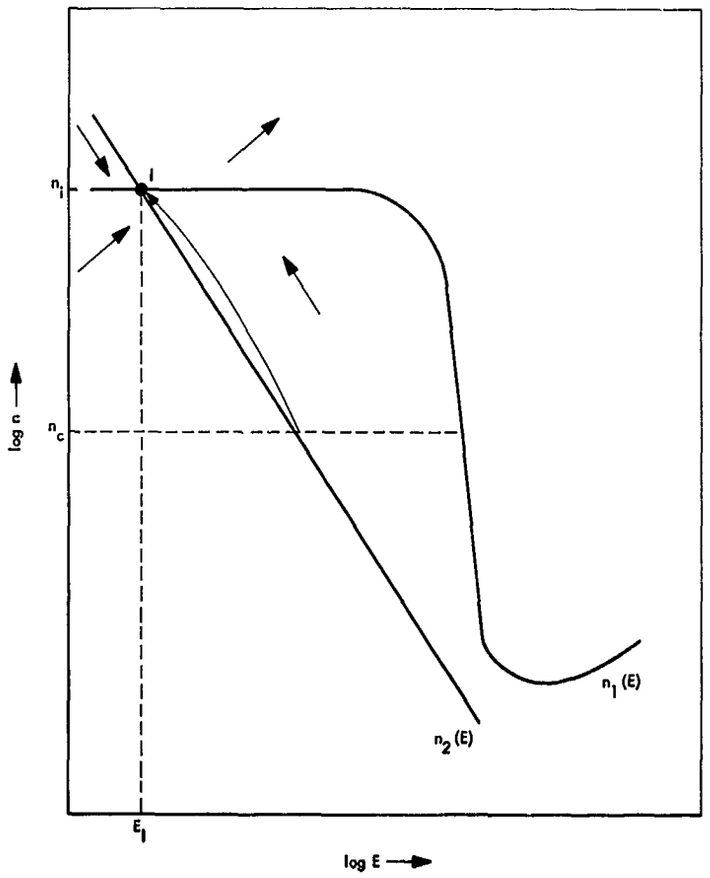

Fig. 5. Symbolized field of direction with charge-neutrality curve $n_1(E)$ and drift-current curve $n_2(E)$

cathode to the edge of the depletion region away from the cathode. Over the rest of the crystal length, the solution curve "stays" near the singular point I, which corresponds to the trivial homogeneous solution $E_I = V_a/L$ where V_a is the applied voltage and L is the electrode separation.

The type of contact at the anode is not important for this investigation; however, if the anode is a neutral contact, the solution curve (Fig. 5) would end at point I for $x = L$. If the anode happened to be blocking (injecting), the curve would dip down (up) in the direction of the third (first) quadrant to values of carrier concentration and electric field below (above) those at point I.

The corresponding current for the simple case just discussed is shown by point A in Fig. 6. The current is slightly below the value expected for an ohmic cathode because of the voltage drop across the depletion region.

When the applied voltage is further increased, the current density j increases, causing the $n_2(E)$ curve to move further away from the origin until, in the region of *NDC*, a second singular point (*II*) appears and approaches n_c (Fig. 7a). The current begins to saturate as shown by point B in Fig. 6, since the solution curve (again starting near n_c)[1] is forced closer to point *II*, remaining close to the value of field E_{II} for *larger* values of x (Fig. 7c), causing a step-like character to $E(x)$, i.e., two field strengths can exist simultaneously. The corresponding carrier density distribution is shown in Fig. 7b. The high-field domain increases in width with further increasing voltage until it reaches the anode (point C in Fig. 6). At this voltage, point *II* is exactly at n_c and a homogeneous solution is obtained: $n = n_c$ and $E = E_{II}$ for all x. The case of higher applied voltages involving domains attached to the anode and the point *III* will not be discussed here.

The values of E_I and E_{II} can be experimentally determined by using the approximation

$$E_{II}l + E_I(L - l) = V_a \tag{4}$$

where l is the domain width. Plotting l versus V_a for a fixed temperature and light intensity yields a straight line with a slope $E_{II} - E_I \cong E_{II}$. The field E_I, which is found to be much less than E_{II} can also be found from the voltage V_0 at which the current in the forward direction equals the saturation current in the reverse direction:

$$E_I = \frac{V_0 - V_0'}{L} \tag{5}$$

where V_0' is the small voltage drop across the barrier. What is most important for our analysis of the barrier height in CdS is that E_{II} is the maximum field within the crystal, that n_{II} is the minimum carrier density, and that the smallest gradients of n and E must lie close to the

[1]The separation of n_c and n_{II} in Fig. 7a is greatly exaggerated on the logarithmic scale used. It will be shown later that $n_c \approx n_{II}$.

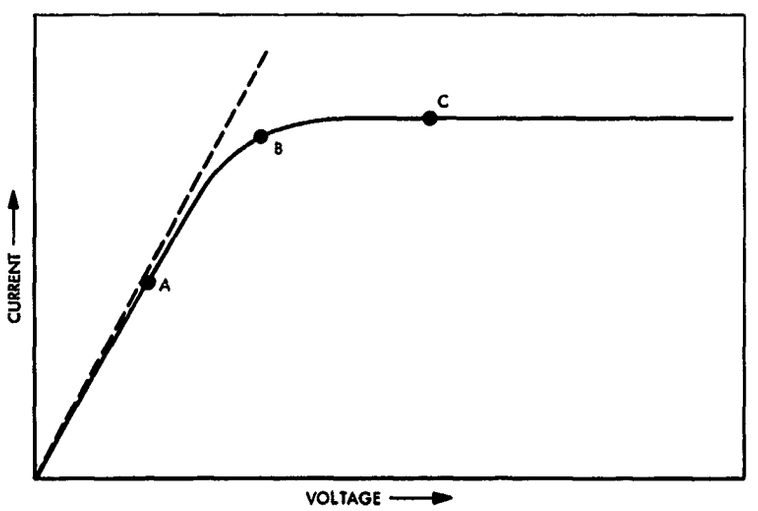

Fig. 6. Reverse current–voltage characteristic in CdS exhibiting stationary high-field domains

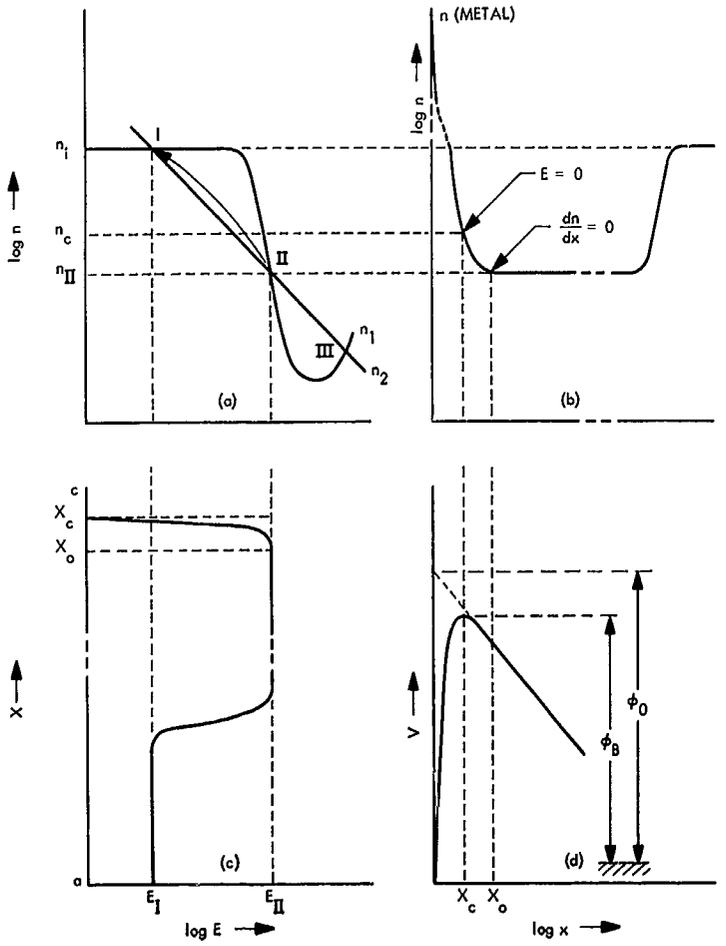

Fig. 7. Carrier concentration vs x and *E*, electric field vs x, and the potential barrier near the cathode

cathode. Thus, the diffusion current can be neglected within the domain and n_{II} can be calculated from E_{II} and the measured saturation current j_s using the relation

$$j_s = qn_{II}\mu E_{II} \tag{6}$$

The expected shape of the barrier is shown in Fig. 7d. At x_c (about 50 A) where the surface field is cancelled by the field due to image forces, the current is given by the diffusion current

$$j = -\mu kT\left(\frac{dn}{dx}\right)_{x=x_c} \tag{7}$$

which increases with smaller x until the maximum diffusion current is attained. This current is called the thermionic current and is given by (Ref. 5)

$$j_{th} = \frac{qv_{th}}{(6\pi)^{1/2}} N_c \exp\left(-\frac{\phi_B}{kT}\right) \tag{8}$$

where v_{th} is the thermal velocity of the electrons in the semiconductor. The saturation current densities obtained in this investigation are far larger than one would calculate from Eq. (8) using values of ϕ_B published in Ref. 1, leading to the conclusion that the barrier height is considerably reduced in CdS under conditions of photoconduction. Large tunneling currents could be another explanation. However, this possibility has been explored[2] and it was concluded that the required buildup of positive space charge at the barrier is not possible in these crystals.

[2]Böer, K. W., Dussell, G. A., and Voss, P., "Experimental Evidence for a Reduction of the Work Function of Blocking Gold Contacts with Increasing Photocurrents in CdS," to be published in *Phys. Rev.*

From Eqs. (1), (6), and (8), we have

$$n_c = (6\pi)^{1/2} \frac{\mu E_{II}}{v_{th}} n_{II} \tag{9}$$

Since $\mu E_{II} \approx v_{th}$ for the values of E_{II} found experimentally, $n_c \approx 5\, n_{II}$ at most.

In this calculation, and in the use of Eq. (6) for determining n_{II}, the value of the electron mobility is assumed constant up to $E = 40$ kV/cm and to decrease as $1/E$ above 40 kV/cm because of optical phonon scattering of the hot electrons (Ref. 5).

The barrier height of Au electrodes evaporated on CdS crystals which have been exposed to air has been recently determined (Footnote 2). However, it is very desirable to obtain results on vacuum-cleaved surfaces in order to eliminate possible interface effects. The results presented in *Subsection 3* have been performed on such crystals.

3. Experimental Arrangement

The CdS crystals were purchased from the University of Delaware's Department of Physics, where they were grown by sublimation and subsequently doped with Ag and Al by a heat treatment at 900°C for 3 hr. The platelets, whose thickness ranged from 0.05 to 0.10 mm, were initially cut into long slices about 0.5-mm wide with a wire saw. These slices were then mounted in wax on a glass plate with a short section exposed over the edge. This end was cleaved in the vacuum evaporater while the metal to be used as the cathode was being evaporated. Only samples which cleaved *below* the wax line were used, assuring that no metal was deposited on the sides. The remaining slice was then removed by dissolving the wax in benzene and broken to give a length of 0.5 to 1.0 mm. The ohmic contact at the opposite end (anode) was later formed by evaporating indium while the sample was heated to 120°C.

The crystals were mounted in clear epoxy between two thin glass plates so that up to 3000 V could be applied without discharges taking place across the surface. Silver paint was used to form leads to the electrodes. The sample was placed in a windowed double-walled glass dewar that allowed the temperature to be varied between 155°K and room temperature by using a resistance heater and liquid nitrogen at the opposite end of a cold finger.

The crystal was illuminated normal to the largest surface with a beam of monochromatic light with a photon energy equal to the bandgap (511 to 495 nm depending on the temperature). The monochromator slits were set to give a band pass of 6 nm and maximum light intensity of 5×10^{16} photons/cm²/s as measured with a Hilger–Schwarz thermopile. Light intensity was reduced by using calibrated neutral density filters.

The use of band-gap light enables one to see the stationary high-field domain (Fig. 8) because of the Franz–Keldysh effect. This effect, in which the fundamental absorption edge is shifted by a high electric field toward lower energies, is due to the fact that, in the presence of such a field, the electrons of the valence band can penetrate somewhat into the band gap, thus allowing optical transitions to occur to similar states below the conduction band edge. The absorption edge shift makes the area where the field-enhanced recombination occurs, i.e., the domain region, appear darker. The sample was viewed through a 20× microscope equipped with a reticle with which the domain length could be measured for a given voltage. This voltage, and the current through the sample as measured by a Keithley picoammeter, were recorded on an x–y recorder.

4. Experimental Results

A number of samples from a single larger crystal were successfully vacuum cleaved and electroded with evaporated Pt, Au, Ag, Ni, Cu, and Sn. Measurements of the reverse current–voltage characteristics up to 3000 V (saturation occurs at 200–300 V), or for forward currents up to 3×10^{-5} A, were made at some selected temperatures and light intensities. Input power was kept below 1mW to prevent heating the sample. The reverse current–voltage characteristics were always similar to Fig. 6 with the saturation current typically around 10^{-6} A ($j_s \approx 10^{-2}$ A/cm²) at $T = 155$°K. The current at higher temperatures (220–295°K) was actually lower than the current at the lowest temperatures due to the presence of thermal quenching in the photoconductor.

Where possible, the domain width as a function of applied voltage was measured for these samples. A decreasing Franz–Keldysh effect (which is proportional to T^{-2}) made it difficult to see domains at the higher temperatures except for metals with values of E_{II} above about 80 kV/cm. Figure 9 shows the domain–voltage dependence for Au at $T = 155$°K and various light intensities with $I_0 = 5 \times 10^{16}$/cm²/s. The slopes (equal to $E_{II} - E_I$) ranged 122–83 kV/cm for this metal contact. Since E_I is less than 1 kV/cm, these slopes were used to approximate E_{II} in Eq. (6).

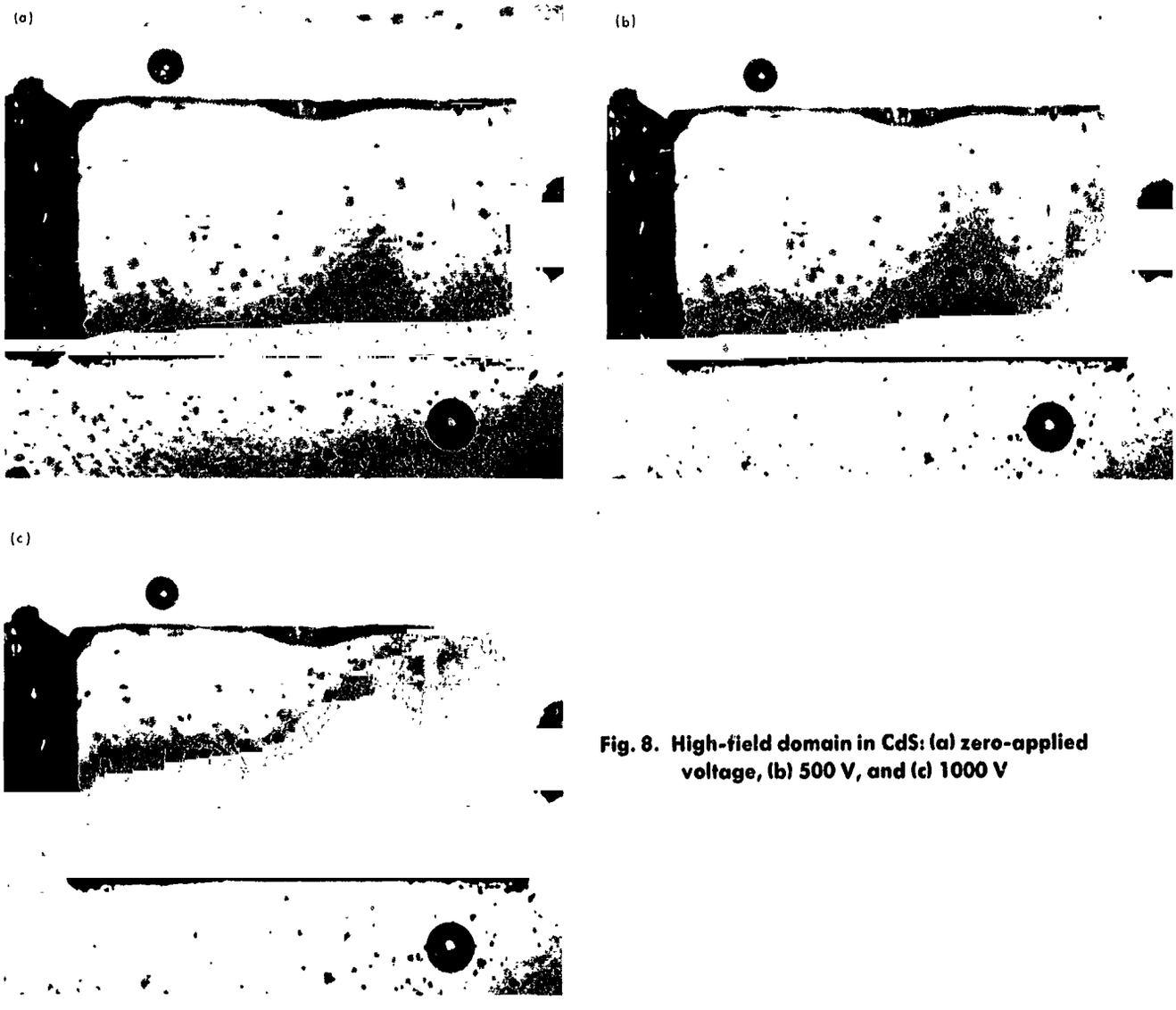

Fig. 8. High-field domain in CdS: (a) zero-applied voltage, (b) 500 V, and (c) 1000 V

The Hall mobility field dependence was obtained from Fig. 10 where the low-field values were obtained from Ref. 6. Above 40 kV/cm, the mobility was assumed to decrease as $1/E$ (Ref. 7).

The values of n_c obtained from the analysis described earlier were typically 10^7–10^{10} cm^{-3} depending on the metal contact, temperature, and light intensity. These values are lower (as expected) than the bulk low-field density n_i by about 10^2–10^3.

Values of the effective barrier heights for CdS (in eV) were then calculated using Eq. (1) and the results for a constant photon flux density of 5×10^{15} (cm^{-2} sec^{-1}) are given in Table 1. It is seen that there are relatively small differences between the metals at any one temperature. Except for Pt, there does seem to be some ordering according to the electronegativity of the metal, but the differences are only hundredths of a volt as compared to tenths of a volt differences in the metal electronegativity (or

Table 1. Barrier heights for CdS

Metal	Electro-Negativity	155°K	180°K	220°K	255°K	295°K
Au	2.4	0.30	0.35	0.42	0.47	0.53
Pt	2.2	0.28	0.33	0.36	—	0.50
Ag	1.9	—	0.34	—	0.47	0.53
Cu	1.9	0.27	0.32	—	0.44	—
Ni	1.8	—	0.31	0.37	—	—
Sn	1.8	0.26	0.29	0.35	—	—

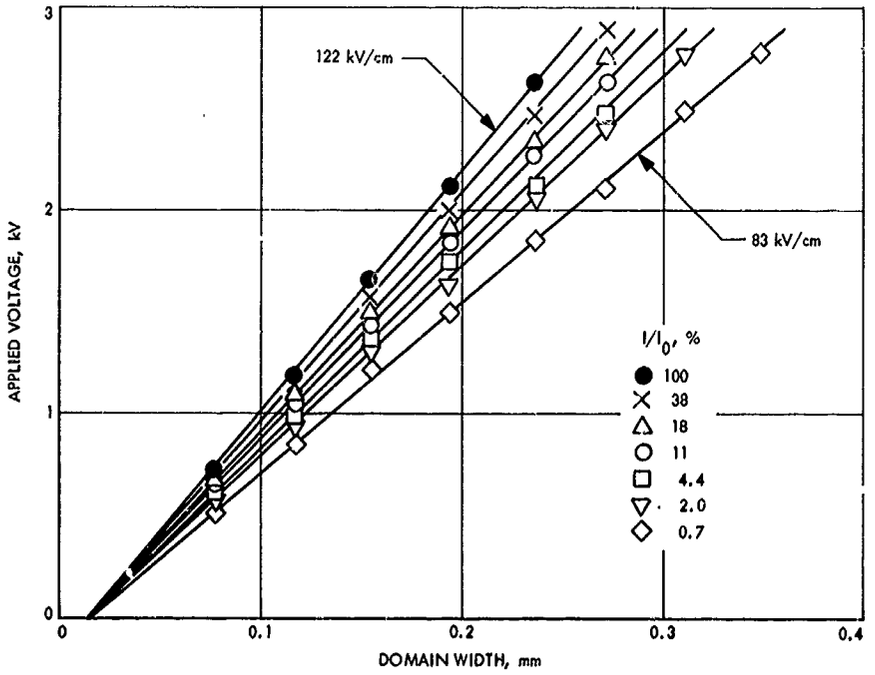

Fig. 9. Domain width vs applied voltage

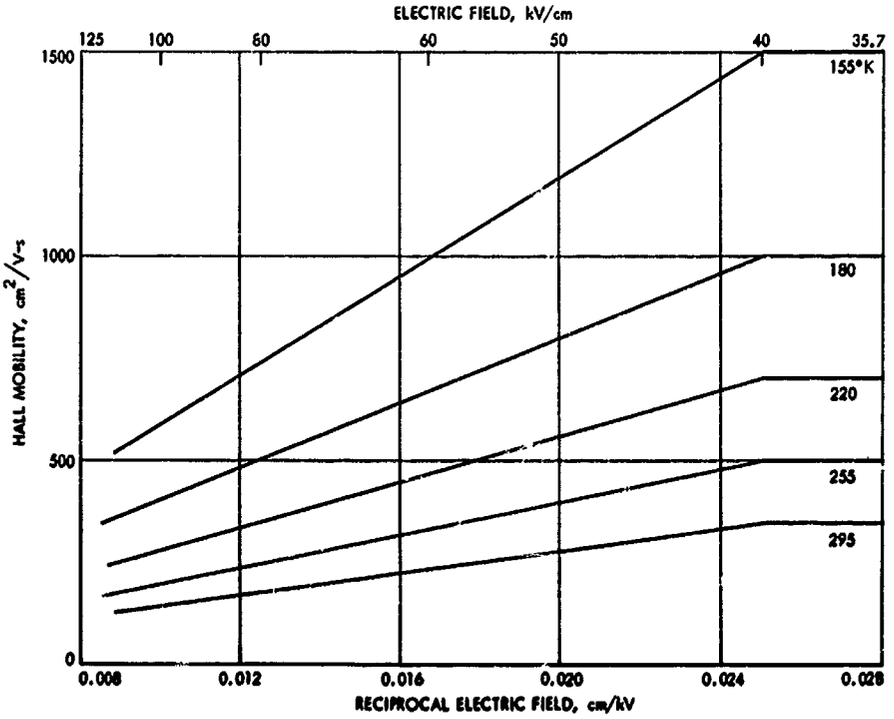

Fig. 10. Assumed field dependence of mobility in CdS

work function). Some differences between the values in Table 1 and published values for lower resistivity CdS were mentioned in the introduction.

The barrier-height temperature dependence observed in the table is shown in Fig. 11 for three of the metals where it is seen that a linear relationship holds.

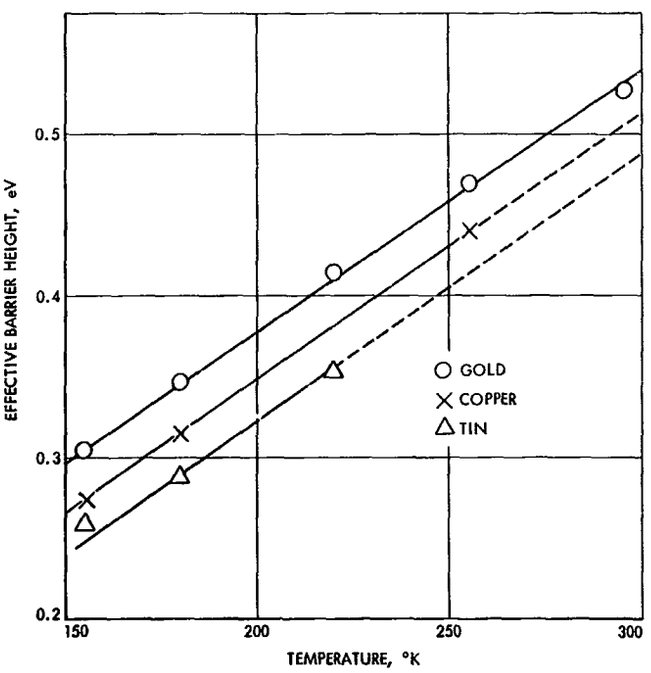

Fig. 11. Temperature dependence of barrier heights on photoconducting CdS for Au, Cu, and Sn

The barrier-height light dependence on CdS for Au and Cu is shown in Fig. 12. Actually, the varying light intensity is only the means to control the amount of photocurrent flowing through the contact, and it is more reasonable conclude that the barrier height, as measured by the high-field-domain technique, is being affected by the amount of current flow and not directly by the photon flux.

5. Conclusions

In contrast to the situation in nonphotoconducting CdS, barrier heights of blocking contacts on photoconducting CdS depend strongly on temperature and the amount of photocurrent flowing through the contact. In addition, the barrier heights, as measured by the high-field-domain technique, are considerably lower in magnitude than those reported in the literature for semiconducting CdS, allowing considerably higher currents through the contacts, and, thus, higher gain factors than would be expected from the earlier and higher barrier heights. An explanation of this unexpected result is not apparent at this time and may involve subtle changes in the dipole layer at the metal–CdS interface due to the presence of the relatively high photocurrents possible in CdS.

Determination of the barrier heights by more conventional techniques (e.g., by photoresponse measurements) would be very desirable, especially for photocurrents lower than those used in this investigation. However, impurity photoconduction would mask out internal photoemission from the metal contact. Differential capacitance measurements also have their difficulties because of the high impedance of these samples.

References

1. Spitzer, W. G., and Mead, C. A., "Barrier Height Studies on Metal-Semiconductor Systems," *J. Appl. Phys.*, Vol. 34, p. 3061, 1963.
2. Böer, K. W., and Voss, P., "Stationary High-Field Domains in the Range of Negative Differential Conductivity in CdS Single Crystals," *Phys. Rev.*, Vol. 171, p. 899, 1968.
3. Böer, K. W., and Quinn, P. L., "Inhomogeneous Field Distribution in Homogeneous Semiconductors having an *N*-Shaped Negative Differential Conductivity," *Phys. Stat. Sol.*, Vol. 17, p. 307, 1966.
4. Böer, K. W., Döhler, G., Dussell, G. A., and Voss, P., "Experimental Determination of Changes in Conductivity with Electric Field, Using a Stationary High-Field Domain Analysis," *Phys. Rev.*, Vol. 169, p. 700, 1968.
5. Spenke, E., *Electronic Semiconductors*, p. 84. McGraw-Hill Book Company, Inc., New York, 1958.
6. Devlin, S. S., Appendix to Shiozawa, L. R. and Jost, J. M., "Research on II–VI Compound Semiconductors," Final Technical Report for Contract AF 33(657)-7399. USAF Aeronautical Research Laboratories, Wright–Patterson Air Force Base, Ohio, 1965.
7. Böer, K. W., and Bogus, K., "Electron Mobility of CdS at High Electric Fields," *Phys. Rev.*, Vol. 174, 1968.

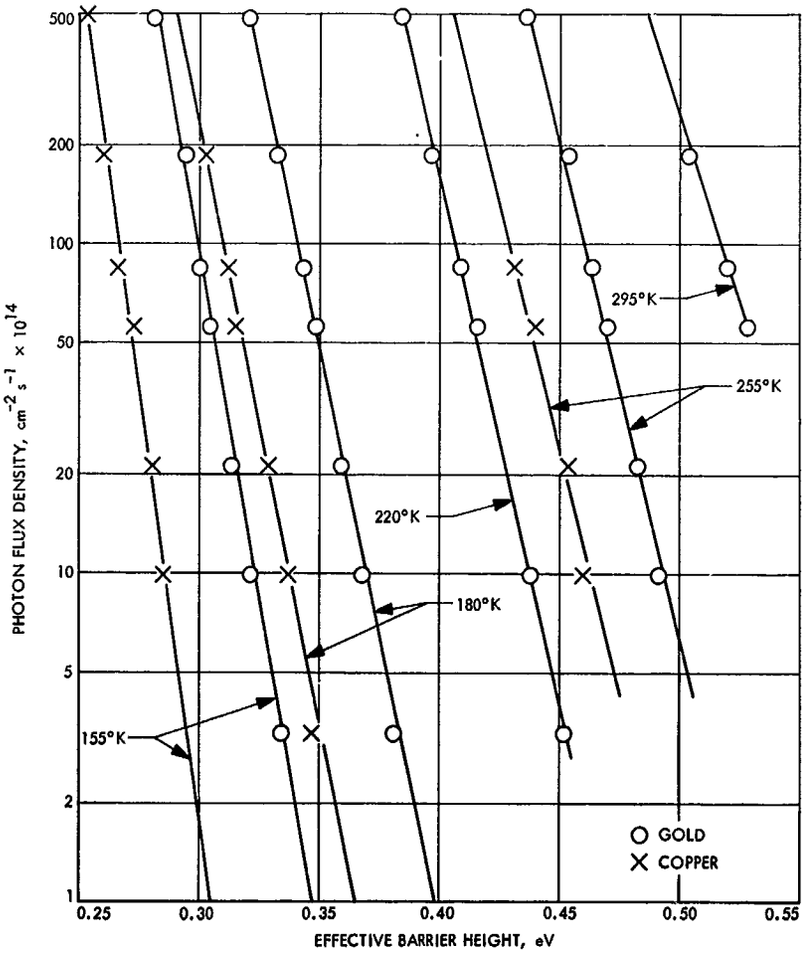

Fig. 12. Barrier-height light dependence on photoconducting CdS for Au and Cu